

AD-A241 690



USAFA-TR-91-12

ORBIT DETERMINATION ERROR ANALYSIS FOR AN INTERIOR LIBRATION POINT ORBIT IN THE SUN-EARTH+MOON ELLIPTIC RESTRICTED THREE-BODY PROBLEM

STEVEN C. GORDON, LT COL, USAF

DEPT OF MATHEMATICAL SCIENCES

SEPTEMBER 1991

FINAL REPORT

**DTIC
ELECTE
OCT. 08 1991
S B D**

APPROVED FOR PUBLIC RELEASE; DISTRIBUTION UNLIMITED



91-12550



**DEAN OF THE FACULTY
UNITED STATES AIR FORCE ACADEMY
COLORADO 80840**

REPORT DOCUMENTATION PAGE

Form Approved
OMB No 0704-0188

Public reporting burden for this collection of information is estimated to average 1 hour per response, including the time for reviewing instructions, searching existing data sources, gathering and maintaining the data needed, and completing and reviewing the collection of information. Send comments regarding this burden estimate or any other aspect of this collection of information, including suggestions for reducing this burden, to Washington Headquarters Services, Directorate for Information Operations and Reports, 1215 Jefferson Davis Highway, Suite 1204, Arlington, VA 22202-4302, and to the Office of Management and Budget, Paperwork Reduction Project (0704-0188), Washington, DC 20503.

1. AGENCY USE ONLY (Leave blank)		2. REPORT DATE Sep 7, 1991	3. REPORT TYPE AND DATES COVERED Final	
4. TITLE AND SUBTITLE Orbit Determination Error Analysis for an Interior Libration Point Orbit in the Sun-Earth+Moon Elliptic Restricted Three-Body Problem			5. FUNDING NUMBERS PR 37731G	
6. AUTHOR(S) Steven C. Gordon, Lt Col, USAF				
7. PERFORMING ORGANIZATION NAME(S) AND ADDRESS(ES) Department of Mathematical Sciences United States Air Force Academy, Colorado 80840			8. PERFORMING ORGANIZATION REPORT NUMBER USAFATR 91-12	
9. SPONSORING/MONITORING AGENCY NAME(S) AND ADDRESS(ES) Frank J. Seiler Research Laboratory United States Air Force Academy, Colorado 80840			10. SPONSORING/MONITORING AGENCY REPORT NUMBER	
11. SUPPLEMENTARY NOTES Research conducted under the direction of Prof K. C. Howell, School of Aeronautics and Astronautics, Purdue University				
12a. DISTRIBUTION/AVAILABILITY STATEMENT			12b. DISTRIBUTION CODE	
13. ABSTRACT (Maximum 200 words) A spacecraft in a libration point orbit between the Earth and the Sun can be useful to study the interaction of the Sun's corona with the terrestrial environment and will be of great scientific value. However, the spacecraft in such an orbit will drift from the nominal (unstable) path, and the forces individually have some level of uncertainty. Both range and range-rate tracking also include some inaccuracy in the data obtained. The accumulated error in the spacecraft's position and velocity relative to the nominal path after a predetermined period of tracking can be measured. This error, or uncertainty, in the spacecraft state is measured through simulations commonly referred to as orbit determination error analysis. The specific error analysis method used here is covariance analysis; the covariance matrix, after a predetermined period of tracking along the nominal path, contains the state uncertainties (state vector element variances) along its diagonal.				
14. SUBJECT TERMS Error analysis, covariance analysis, least squares, Kalman filter, batch weighted least squares, libration points, three-body problem, spacecraft orbits			15. NUMBER OF PAGES 97	
17. SECURITY CLASSIFICATION OF REPORT UNCLASSIFIED			18. SECURITY CLASSIFICATION OF THIS PAGE UNCLASSIFIED	19. SECURITY CLASSIFICATION OF ABSTRACT UNCLASSIFIED
20. LIMITATION OF ABSTRACT				

USAFA-TR-91-12

Technical Review by Captain Rich Schooff
Department of Mathematical Science
USAFA Academy, Colorado 80840

Technical Review by Lt Col Daryl G. Boden
Department of Astronautics
USAF Academy, Colorado 80840

Editorial Review by Lt Col Donald C. Anderson
Department of English
USAF Academy, Colorado 80840

This research report entitled "Orbit Determination Error Analysis For An Interior Libration Point Orbit In The Sun-Earth+Moon Elliptic Restricted Three-Body Problem" is presented as a competent treatment of the subject, worthy of publication. The United States Air Force Academy vouches for the quality of the research, without necessarily endorsing the opinions and conclusions of the author.

This report has been cleared for open publication and public release by the appropriate Office of Information in accordance with AFM 190-1, AFR 12-30, and AFR 80-3. This report may have unlimited distribution.

Robert K. Morrow Jr.
ROBERT K. MORROW JR., Lt Col, USAF
Director of Research

LE AUG 91
Dated



Accession For	
NTIS GRA&I	<input checked="checked" type="checkbox"/>
DTIC TAB	<input type="checkbox"/>
Unannounced	<input type="checkbox"/>
Justification	
By	
Distribution/	
Availability Codes	
Dist	Avail and/or Special
A-1	

ORBIT DETERMINATION ERROR ANALYSIS FOR
AN INTERIOR LIBRATION POINT ORBIT
IN THE SUN-EARTH+MOON ELLIPTIC
RESTRICTED THREE-BODY PROBLEM

Lieutenant Colonel Steven C. Gordon,
Assistant Professor
Department of Mathematical Sciences

PREFACE

Bounded nominal paths can be constructed in the vicinity of the interior equilibrium point (sometimes called a libration or Lagrange point) for the Sun-Earth+Moon Elliptic Restricted Three-Body Problem. Numerical integration is used to generate the periodic or quasi-periodic reference trajectories in this effort, and the numerical data is then curve fit using a cubic spline routine. The force model used in this effort includes the gravitational attractions of the Sun plus the Earth+Moon barycenter (treated as one body), along with the centrifugal force associated with rotation of the system. Solar radiation pressure force is also included. A spacecraft in a libration point orbit between the Earth and the Sun can study the interaction of the Sun's corona with the terrestrial environment and will be of great scientific value.

However, the spacecraft in such an orbit will drift from the nominal (unstable) path, and the forces individually have some level of uncertainty. Both range and range-rate tracking also include some inaccuracy in the data obtained. The accumulated error in the spacecraft's position and velocity relative to the nominal path after a predetermined period of tracking can be measured. This error, or uncertainty, in the spacecraft state is measured through simulations commonly referred to as orbit determination error analysis. The specific error analysis method used here is covariance analysis; the covariance matrix, after a predetermined period of tracking along the nominal path, contains the state uncertainties (state vector element variances) along its diagonal.

This effort is supported by the Frank J. Seiler Research Laboratory and has been conducted as doctoral research under the direction of Professor K.C. Howell, School of Aeronautics and Astronautics, Purdue University, West Lafayette, Indiana.

TABLE OF CONTENTS

	Page
TABLE OF CONTENTS.....	iii
LIST OF FIGURES.....	iv
LIST OF TABLES.....	v
INTRODUCTION.....	1
CHAPTER 1: BACKGROUND.....	6
A. Elliptic Restricted Three-Body Problem.....	6
B. Coordinate Systems.....	7
C. Equations of Motion.....	9
D. Locations of the Lagrangian Points.....	12
1. The CR3BP.....	12
2. The ER3BP.....	14
E. State Transition Matrix.....	16
F. Bounded Orbits Near Libration Points.....	18
1. Stability of the Libration Points in the CR3BP.....	19
2. Stability of the Libration Points in the ER3BP.....	20
3. Construction of Bounded Collinear Libration Point Orbits.....	20
4. Reference Paths Used in This Work.....	22
5. Curve Fitting the Nominal Path.....	25
CHAPTER 2: ORBIT DETERMINATION ERROR ANALYSIS.....	29
A. Background.....	31
B. The Kalman Filter.....	33
C. Batch Weighted Least Squares.....	45
D. Consider Covariance Analysis.....	48
CHAPTER 3: ORBIT DETERMINATION ERROR ANALYSIS RESULTS.....	60
A. Survey of Input Error Levels Used in Other Research.....	61
B. Kalman Filter Results.....	63
C. Comparison of Weighted Batch Least Squares and Kalman Filters.....	70
D. Consider Covariance Analysis Results.....	72
E. Computing Error Levels for Station-Keeping Simulations....	74
F. Probability Distribution of the Resulting Errors.....	80
LIST OF REFERENCES.....	94

LIST OF FIGURES

Figure	Page
1-1. Coordinate Systems With Barycenter Origin.....	8
1-2. Lagrange Point Locations in the Scaled CR3BP.....	13
1-3. Lagrange Point Locations in the Scaled ER3BP.....	15
1-4. Three Orthographic Views of a Lissajous Orbit.....	23
1-5. Three Orthographic Views of a Halo-Type Orbit.....	24
1-6. Time Series Plots of Three Lissajous Position States.....	27
1-7. Time Series Plots of Three Lissajous Velocity States.....	28
3-1. Kalman Filter Plots for the y State Variable.....	64
3-2. Kalman Filter Plots for the y State Variable when Added System Noise is Used.....	66
3-3. Gain Element 2,2.....	68
3-4. Gain Element 2,2 When System Noise is Included in the Filter...	69
3-5. Histogram of the x Excursion From the Integrated Path.....	82
3-6. Histogram of the y Excursion From the Integrated Path.....	83
3-7. Histogram of the z Excursions From the Integrated Path.....	84
3-8. Histogram of the x Velocity Excursion From the Integrated Path.....	85
3-9. Histogram of the y Velocity Excursion From the Integrated Path.....	86
3-10. Histogram of the z Velocity Excursion From the Integrated Path.....	87
3-11. Histogram of y Excursion From Integrated Path Including Observed Frequencies.....	92
3-12. Histogram of y Excursion From the Integrated Path Using Gaussian Expectations.....	93

LIST OF TABLES

Table	Page
1. Survey of Error Analysis Input Errors.....	62
2. Comparison of Batch Least Squares and Kalman Filters.....	70
3. Comparison of Consider Covariance Error Analysis Results.....	74
4. Error Analysis Results for a Halo-Type Orbit: Range in the Standard Deviation for Various Levels of Solar Reflectivity Uncertainty.....	78
5. Error Levels Produced from Error Analysis Studies.....	79
6. Comparison of Error Analysis Results from Several Sources.....	79
7. Results of the Error Analysis Goodness of Fit Tests.....	89
8. Hypothesis Test for Zero Error Means.....	90

INTRODUCTION

With the expansion of space exploration programs worldwide, interest has increased in the design of innovative, complex, and yet low-cost spacecraft trajectories that meet demanding mission requirements. In most of the missions flown in the last few decades, the spacecraft spent the majority of the flight time in a force environment dominated by a single gravitational field. For the preliminary mission analysis in these cases, additional attracting bodies and other forces could be modeled, when required, as perturbing influences. Analysis of some recently proposed and more adventurous missions, such as those involving libration point orbits, will require dynamic models of higher complexity, since at least two gravitational fields are of nearly equal influence on the spacecraft throughout the majority of the mission. Thus, trajectories determined for a system consisting of numerous gravitational forces have been of particular theoretical and practical interest in recent years.

One type of many-body problem, motion within a three-body system of forces, has a wide range of applications. The general problem of three bodies assumes that each body has finite mass and that the motion is a result of mutual gravitational attraction. When the mass of one of the three bodies is assumed to be sufficiently small (infinitesimal) so that it does not affect the motion of the other two bodies (primaries) in the system, the "restricted three-body problem" results. The primaries can be further assumed to be moving in known elliptic or circular orbits about their common center of mass. Therefore, the elliptic restricted three-body problem, where the primaries are assumed to be in known elliptic orbits, may be considered a reasonably approximate model for a spacecraft moving within the gravitational fields of the Sun and the Earth, for instance.

In the formulation of the restricted three-body problem, one mass is defined as infinitesimal relative to the remaining two masses (primaries). The primaries, unaffected by the infinitesimal mass, move under their mutual gravitational attractions. In the elliptic restricted three-body problem (ER3BP), the primaries are assumed to move on elliptic paths. If the eccentricity of the primaries' orbit is assumed to be zero, the circular restricted three-body problem (CR3BP) results. Even for known primary motion, however, a general, closed-form solution for motion of the third body of infinitesimal mass does not exist. In the restricted three-body problem (ER3BP or CR3BP), five equilibrium (libration) solutions can be found. These equilibrium points, sometimes also referred to as Lagrange points, are particular solutions of the equations of motion governing the path of the infinitesimal mass moving within the gravitational fields of the primaries.

The equilibrium points are defined relative to a coordinate system rotating with the primaries. At these locations, the forces on the spacecraft are in equilibrium. These forces include the gravitational forces from the massive bodies and the centrifugal force associated with the rotation of the system. (The addition of solar radiation pressure to the force model changes the locations of the five Lagrange points, although they can still be defined, and these solar radiation effects are discussed in Gordon^[1].) The libration points are located in the plane of primary rotation. Three of the libration points are on the line between the two massive bodies, and one of these collinear points is interior to the primaries. The last two points are at the vertices of two equilateral triangles in the plane of primary rotation. The triangles have a common base that is the line between the primary masses.

For the CR3BP, the five libration points are stationary relative to the rotating reference frame. If the problem is generalized to the ER3BP, the libration points pulsate as the distance between the primaries varies with time. In both the circular and elliptic restricted problems, two-dimensional and three-dimensional trajectories, both periodic and quasi-periodic paths, can be computed in the vicinity of these libration points.

Three-dimensional, periodic "halo" orbits in the vicinity of the collinear libration points have been studied since the late 1960s. Early work concerning these orbits was motivated by studies related to exploring the far side of the Moon. These studies were completed in support of the planned Apollo 18 lunar exploration mission that was later canceled. Robert Farquhar coined the term "halo" to describe a three-dimensional, periodic orbit near a libration point on the far side of the Moon in the Earth-Moon system.^[2] These orbits were designed to be large enough so that the spacecraft would be constantly in view of the Earth and would thus appear as a halo around the Moon. A communications station in this type of orbit could maintain constant contact between the Earth and a lunar experimentation station on the far side of the Moon.^[3]

Quasi-periodic orbits near libration points are also currently of great research interest. The variations in size and shape that a quasi-periodic orbit can exhibit may add valuable flexibility for mission planning. This type of bounded, three-dimensional libration point trajectory is called a Lissajous orbit since specific planar projections of these quasi-periodic trajectories may look like a special type of "Lissajous" curve. Physicist Jules Antoine Lissajous (1822-1880) investigated curves that were generated by compounding simple harmonic motions at right angles, and he delivered a paper on this subject to the Paris Academy of Sciences in 1857. Nathaniel Bowditch of Salem, Massachusetts, had conducted some similar work in 1815. Lissajous curves have a wide variety of shapes that depend on the frequency, phase, and amplitude of the orthogonal components of the motion.^[4,5] When the in-plane and the (orthogonal) out-of-plane frequencies of the linearized motion are nearly (but not) equal, the resulting path is typically called a Lissajous trajectory.

A method to generate approximations for this type of quasi-periodic orbital path was developed analytically by Farquhar and Kamel in 1973.^[6] They derived a third-order approximate analytic solution for a translunar libration point orbit in the Earth-Moon ER3BP that also included solar gravity perturbations. In 1975, Richardson and Cary then developed a fourth-order analytic Lissajous approximation

in the Sun-Earth+Moon barycenter system.^[7] The notation "Earth+Moon" indicates that the Earth and the Moon are treated as one body with mass center at the Earth-Moon barycenter. In consideration of the lunar perturbation, Farquhar has shown that the accuracy of solutions in the Sun-Earth CR3BP can be enhanced if the collinear libration points are defined along the line between the Sun and the center of mass of the Earth and the Moon.^[8] Since 1975, a few researchers have considered methods to numerically generate Lissajous trajectories, but the lack of periodicity of a Lissajous path complicates numerical construction of bounded trajectories. Howell and Pernicka have developed a numerical technique for determination of three-dimensional, bounded Lissajous trajectories of arbitrary size and duration.^[9-14] Orbits computed with their method are used in this effort to define the nominal path near which the spacecraft will be maintained.

Trajectory determination for a spacecraft that moves under the influence of a two-body system of forces will, however, be affected by many sources of error, including tracking errors, modeling uncertainty, and, possibly, control input errors. Orbit determination error analysis seeks to quantify the impact of the numerous errors that affect the motion of the spacecraft. The result of the error analysis is a determination of the spacecraft position and velocity uncertainty after some predetermined period of flight during which the spacecraft is affected by both the uncertainties in the forces and the errors in tracking data. The combined magnitude of the errors may be found to vary depending on the size and shape of the spacecraft orbit. A reduction in, or a more accurate estimation of, the magnitudes of the individual errors may be possible and could then lead to a significant reduction in overall vehicle position and velocity uncertainty.

This reduced level of position and velocity uncertainty may, in turn, reduce orbital "maintenance" costs, such as the propellant required to keep the spacecraft near the nominal orbit. The orbital maintenance routine is referred to here as "station-keeping." This cost is, in part, dependent on the accuracy of the tracking information because position updates using inaccurate tracking data may result in inefficient use of control energy and may also lead to unacceptable spacecraft drift from the nominal path. Other error sources may also

affect spacecraft drift from the reference trajectory and, therefore, may increase station-keeping costs.

This research is concerned with quantifying the resulting impact of some of the possible error sources on orbit determination. These investigations use a nominal path for the spacecraft orbit that is numerically computed as a solution in the elliptic restricted three-body problem. Simulated tracking data, including assumed levels of the associated errors, can then be produced. The overall spacecraft position and velocity uncertainties can be computed at a specified epoch and can be compared as functions of various levels of error magnitudes as well as differing orbital shapes and sizes. Using two nominal orbit types and various input parameter errors as a basis, the resulting errors can then be compared. Chapter 1 briefly covers the background of the elliptic restricted three-body problem. Chapter 2 then summarizes three methods of orbit determination error analysis, and, finally, Chapter 3 covers the results obtained. Follow-on research, not included in this effort, can then use the resulting error levels in simulations of various station-keeping algorithms.

CHAPTER 1: BACKGROUND

In this chapter, the elliptic restricted three-body problem and the associated coordinate systems are reviewed; the equations of motion for an infinitesimal mass moving in the gravity fields of two massive bodies are then presented. Next, locations of the libration points are discussed. The state transition matrix and the construction of bounded nominal orbits near the collinear Lagrange points are then summarized. Finally, curve fitting the nominal trajectory is covered. A more thorough discussion of these topics is presented in Gordon.^[1,15]

A. Elliptic Restricted Three-Body Problem

The elliptic restricted three-body problem is a simplification of the general problem of three bodies. In the general three-body problem, each of the three bodies is assumed to be a particle of finite mass and, thus, exerts an influence on the motion of each of the other bodies. Neither the general nor the restricted problem of three bodies has a general closed-form solution. However, when problem simplifications are made, particular solutions can be determined. If the mass of one of the bodies is restricted to be infinitesimal, such that it does not affect the motion of the other two massive bodies (primaries), the restricted three-body model results. The primaries are assumed to be in known elliptic (ER3BP) or circular (CR3BP) orbits about their common mass center (barycenter). The problem can then be completely described by a single second-order vector differential equation with variables appropriately defined for a specified coordinate frame.

B. Coordinate Systems

The two standard coordinate systems used in the analysis of this problem have a common origin at the center of mass (barycenter) of the primaries. Primaries with masses m_1 and m_2 such that $m_1 \geq m_2$ are assumed here, although this distinction is arbitrary. The infinitesimal mass is denoted as m_3 . These masses (m_1, m_2, m_3) correspond to particles situated at points P_1 , P_2 , and P_3 , respectively. The barycenter is denoted as "B," and the resulting arrangement is shown in Figure 1-1. The rotating coordinate system is defined as $x_R y_R z_R$, and the inertial system is identified as $x_I y_I z_I$. Note that both coordinate systems are right-handed, and the x and y axes for both systems are in the plane of motion of the primaries. The x_I axis is, of course, assumed to be oriented in some fixed direction; in this specific formulation of the problem, it is assumed to be parallel to a vector defined with a base point at the Sun and directed toward periaapsis of the Earth's orbit. The rotating x_R axis is defined along the line that joins the primaries and is directed from the larger toward the smaller primary. The z axes are coincident and are directed parallel to the primary system angular momentum vector. The y_R axis completes the right-handed $x_R y_R z_R$ system.

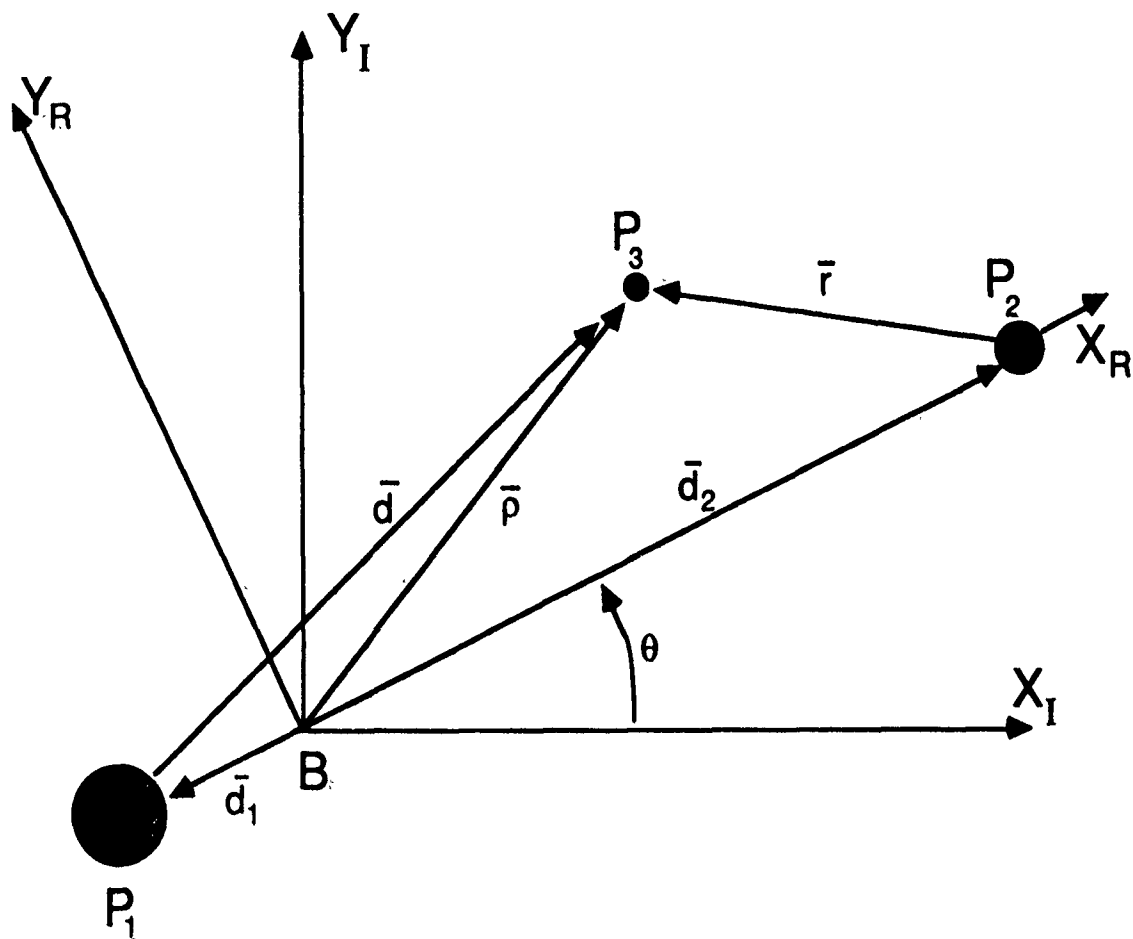


Figure 1-1. Coordinate Systems With Barycenter Origin.

C. Equations of Motion

Newtonian mechanics are used to formulate the equations of motion for m_3 (the spacecraft) relative to B as observed in the inertial reference frame. The sum of the forces on m_3 resulting from both the gravity fields of masses m_1 (the Sun) and m_2 (the Earth-Moon barycenter) and from the solar radiation pressure can be used to produce the following second-order vector differential equation:

$$\ddot{\bar{\rho}} = -G \left(\frac{m_1}{d^3} \right) \bar{d} - G \left(\frac{m_2}{r^3} \right) \bar{r} + \left(\frac{kS}{d^3} \right) \bar{d}. \quad (1-1)$$

The overbar denotes a vector, and primes indicate differentiation with respect to dimensional time. All quantities are dimensional, as appropriate, and the quantity "G" is the universal gravitational constant. The scalars "d" and "r" in equation (1-1) denote the magnitudes of the vectors \bar{d} and \bar{r} , respectively, as depicted in Figure 1-1. The dimensionless scalar "k" is the solar reflectivity constant, and "S" is the solar radiation pressure constant. The formulation of the solar radiation force model and the values for the solar radiation constants are derived from previous work by Bell.^[16] The values of the constants are described in Gordon.^[1]

The position vector $\bar{\rho}$ is written in rotating components as

$$\bar{\rho} = x \hat{x}_R + y \hat{y}_R + z \hat{z}_R \quad (1-2)$$

where $\hat{x}_R, \hat{y}_R, \hat{z}_R$ are unit vectors. The velocity and the acceleration of the spacecraft (particle P_3 with mass m_3) relative to the barycenter B as observed in the inertial reference frame can then be described. The following kinematic expression for $\ddot{\bar{\rho}}$ can be derived:

$$\bar{\rho}'' = (x'' - \theta''y - 2\theta'y' - \theta'^2x)\hat{x}_R + (y'' + \theta''x + 2\theta'x' - \theta'^2y)\hat{y}_R + z''\hat{z}_R. \quad (1-3)$$

Three scaled equations of motion for P_3 can be derived using the following scaling factors:

- (1) The sum of the masses of the primaries equals one mass unit.
- (2) The mean distance between the primaries equals one unit of distance.
- (3) The universal gravitational constant is equal to one unit by proper choice of characteristic time.

The dimensional equations of motion can be simplified and scaled by introducing the characteristic quantities defined above and by introducing the nondimensional mass ratio μ , "psuedo-potential" U , and the scaled solar radiation constant s :

$$\mu = \frac{m_2}{m_1 + m_2} \quad (1-4)$$

and

$$U = \frac{(1-\mu)}{d} + \frac{\mu}{r} + \frac{1}{2} \dot{\theta}^2 (x^2 + y^2) - \frac{k s}{d} \quad (1-5)$$

where the dot denotes the derivative with respect to characteristic time. The scaled solar radiation constant, s , is derived by using the characteristic quantities described above. Then, the vector magnitudes, " d " and " r ," are written in terms of scaled quantities as:

$$d = [(x + \mu R)^2 + y^2 + z^2]^{1/2}, \quad (1-6)$$

$$r = [(x - R + \mu R)^2 + y^2 + z^2]^{1/2}. \quad (1-7)$$

The three scalar second-order differential equations that result can be written in terms of characteristic quantities as

$$\ddot{x} - 2 \dot{\theta} \dot{y} = \frac{\partial U}{\partial x} + \ddot{\theta} y = U_x + \ddot{\theta} y, \quad (1-8)$$

$$\ddot{y} + 2 \dot{\theta} \dot{x} = \frac{\partial U}{\partial y} - \ddot{\theta} x = U_y - \ddot{\theta} x, \quad (1-9)$$

$$\ddot{z} = \frac{\partial U}{\partial z} = U_z. \quad (1-10)$$

If the primaries are assumed to be moving in a circular orbit, equations (1-8), (1-9), and (1-10) reduce to three scalar equations in the simplified form:

$$\ddot{x} - 2\dot{y} = \frac{\partial U}{\partial x} = U_x, \quad (1-11)$$

$$\ddot{y} + 2\dot{x} = \frac{\partial U}{\partial y} = U_y, \quad (1-12)$$

$$\ddot{z} = \frac{\partial U}{\partial z} = U_z. \quad (1-13)$$

The scalar equations can be used to locate the five libration points in the rotating reference frame.

D. Locations of the Lagrangian Points

By using scalar equations (1-11), (1-12), and (1-13) for motion in the CR3BP, the locations of the stationary equilibrium points can be determined. Equations (1-8), (1-9), and (1-10) can be used to determine ratios of distances that are constant in the ER3BP; these ratios are related to the locations of libration points that have been defined in the ER3BP and that "pulsate" with respect to the rotating reference frame as the distance between the primaries varies with time.

1. The CR3BP

In the CR3BP, the five libration points are equilibrium points and are stationary with respect to the rotating coordinate frame, that is, they are locations at which the forces on the third body sum to zero. The arrangement of points and the corresponding nondimensional distances are depicted in Figure 1-2. Note that three of the libration points (L_1 , L_2 , L_3) are collinear with the primaries; one collinear

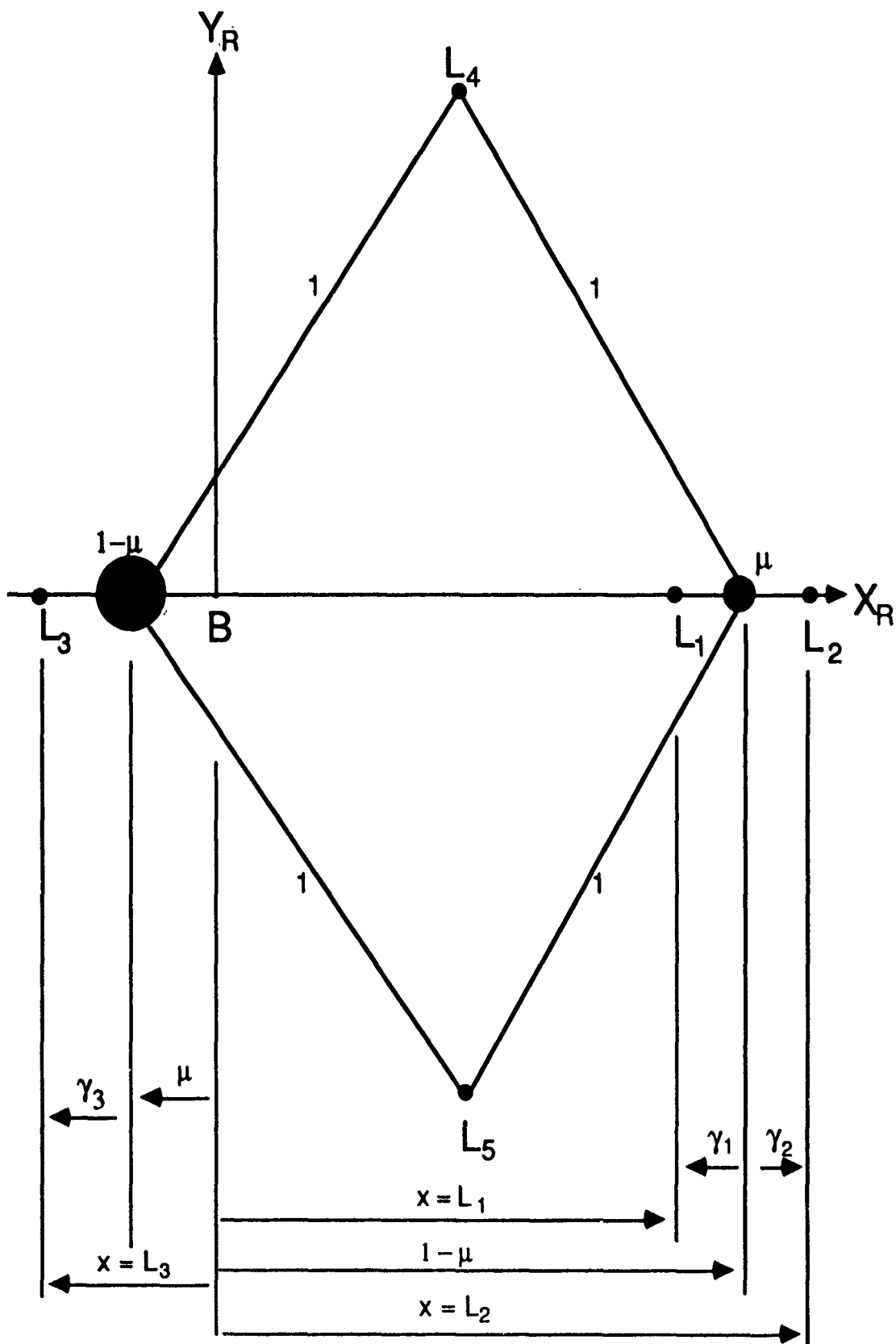


Figure 1-2. Lagrange Point Locations in the Scaled CR3BP.

point (L_1) is interior to the primaries. The remaining two points (L_4 and L_5) are located at the vertices of two equilateral triangles that are in the plane of primary rotation and that have a common base between the primaries.

In the CR3BP, the libration points are stationary in the rotating coordinate frame. Stationary points are defined as points at which the relative velocity and acceleration are zero, such that

$$\dot{x} = \dot{y} = \dot{z} = \ddot{x} = \ddot{y} = \ddot{z} = 0. \quad (1-14)$$

By using equations (1-14) in equations (1-11) through (1-13), the useful conditions $U_x = U_y = U_z = 0$ are found. The three collinear libration points can be readily located by further noting that $y = z = 0$ for the points located on the rotating x_R axis.

2. The ER3BP

Five libration points also exist in the ER3BP, but they are not stationary relative to the rotating frame; rather, the collinear points pulsate along the x_R axis, and the triangular points pulsate relative to both the x_R and the y_R axes as the distance between the primaries varies with time. The equilibrium solutions can be located by using equations (1-8) through (1-10) to find ratios of certain distances that are, in fact, constant in the problem. The collinear libration points in the ER3BP can be found by assuming $\dot{x} \neq 0$, $x \neq 0$, and $\dot{y} = \ddot{y} = \dot{z} = \ddot{z} = y = z = 0$. The relative locations of the libration points in the ER3BP are depicted in Figure 1-3.

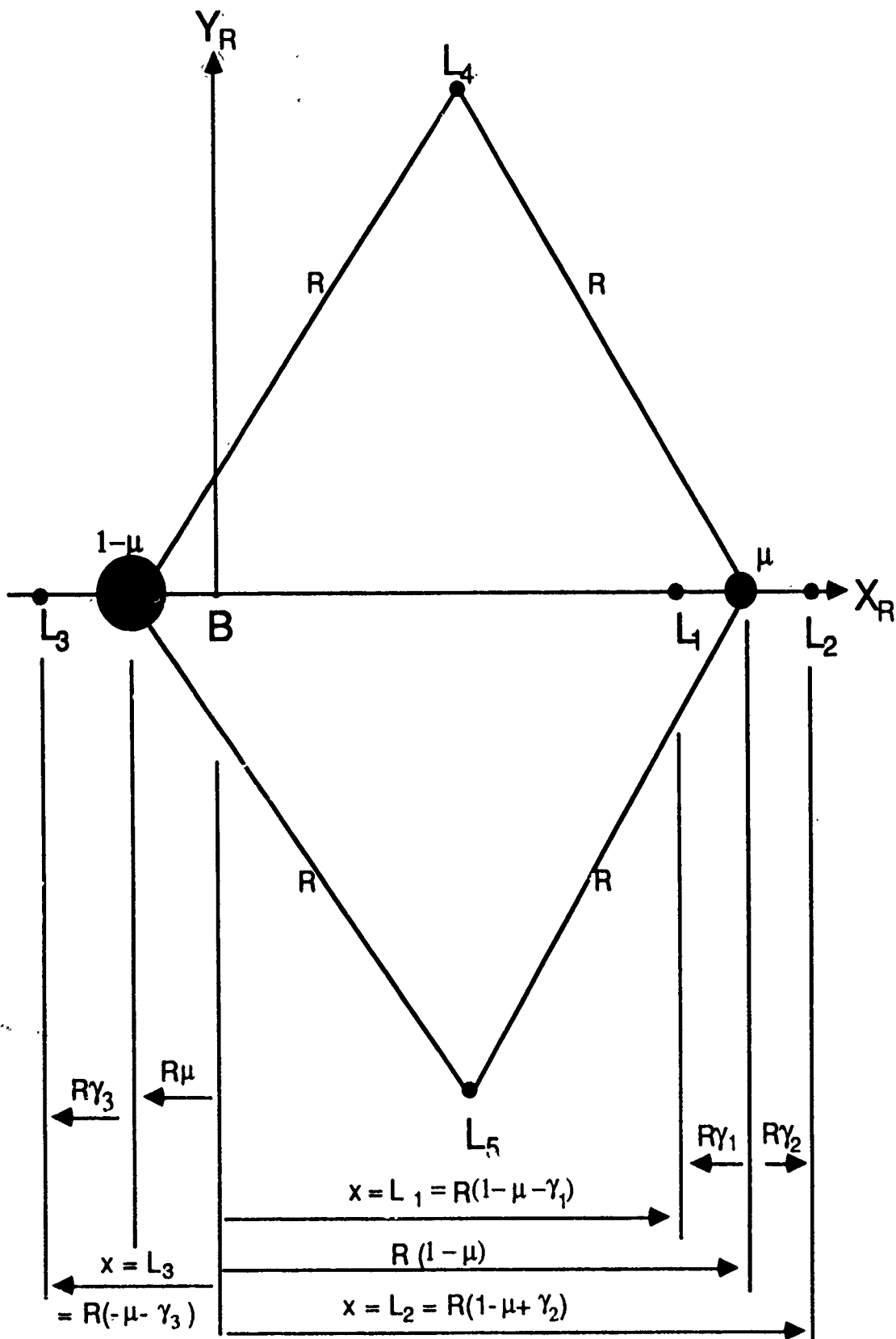


Figure 1-3. Lagrange Point Locations in the Scaled ER3BP.

E. State Transition Matrix

The state transition matrix is used in the calculation of the acceptable nominal trajectory, and it must also be available at varying time intervals along the nominal path for orbit determination error analysis investigations and station-keeping studies. The transition matrix is derived in connection with a linearizing analysis.

The equations of motion for the infinitesimal mass in the ER3BP can be linearized about a reference trajectory (nominal path) that is a solution of the differential equations. The states, three position and three velocity, and the state vector \bar{x} are defined as

$$x_1 = x, x_2 = y, x_3 = z, x_4 = \dot{x}, x_5 = \dot{y}, x_6 = \dot{z}, \quad (1-15)$$

and

$$\bar{x} = [x_1, x_2, x_3, x_4, x_5, x_6]^T. \quad (1-16)$$

The reference trajectory is defined as \bar{x}_{REF} . Therefore, using a Taylor's series approach, the expansion about the reference path is written in the form of the first-order variational equation

$$\frac{d}{dt}(\tilde{x}) = \dot{\tilde{x}} = A(t) \tilde{x} \quad (1-17)$$

where $\tilde{x} = \bar{x} - \bar{x}_{REF}$ is understood to be the vector of residuals relative to the nominal solution, and the matrix $A(t)$ contains the first-order terms in the Taylor's series expansion of the equations of motion about the nominal or reference solution of interest.

Using equations (1-8) through (1-10), $A(t)$ can be expressed as

$$A(t) = \begin{bmatrix} 0 & I \\ U_{rr} + \ddot{\theta}\Omega & 2\dot{\theta}\Omega \end{bmatrix} \quad (1-18)$$

where all four submatrices are dimension 3×3 and

$$U_{rr} = \begin{bmatrix} U_{xx} & U_{xy} & U_{xz} \\ U_{yx} & U_{yy} & U_{yz} \\ U_{zx} & U_{zy} & U_{zz} \end{bmatrix} \quad (1-19)$$

with

$$\Omega = \begin{bmatrix} 0 & 1 & 0 \\ -1 & 0 & 0 \\ 0 & 0 & 0 \end{bmatrix}.$$

In equation (1-19), the notation is simplified for the partial derivatives; for instance

$$\frac{\partial^2 U}{\partial x^2} = U_{xx}.$$

The matrix $A(t)$ can then be evaluated along the reference trajectory.

The vector differential equation (1-17) governing the state variations from the nominal path has a solution of the form

$$\tilde{x}(t) = \Phi(t, t_0) \tilde{x}(t_0) \quad (1-20)$$

where $\Phi(t, t_0)$ is the state transition matrix at time "t" relative to time " t_0 ." The matrix Φ , then, represents the sensitivities of the states at time "t" to small changes in the initial conditions. It is determined by numerically integrating the matrix differential equation

$$\frac{d}{dt} \Phi(t, t_0) = \dot{\Phi}(t, t_0) = A(t) \Phi(t, t_0), \quad (1-21)$$

with initial conditions $\Phi(t_0, t_0) = I$, the 6x6 identity matrix. Thus, the nonlinear equations of motion in (1-8) through (1-10) and the matrix equation (1-21) combine to result in 42 first-order differential equations that can be simultaneously integrated numerically to determine the state vector and its associated transition matrix at any instant of time. The reference trajectories that are of interest in this research are generated by a numerical integration method that uses a differential corrections process developed by Howell and Pernicka.^[9-14] The orbits include solar radiation pressure forces as formulated by Bell^[16] specifically for an orbit associated with the interior Lagrange point in the Sun-Earth system. The numerical integration routines used in this work are fourth- and fifth-order Runge-Kutta formulas available in the 386-Matlab software package.^[17]

F. Bounded Orbits Near Libration Points

The computation of bounded periodic and quasi-periodic orbits in the vicinity of libration points has been of increasing interest during the past 100 years. This section first discusses the stability of the libration points in the CR3BP and the ER3BP. The construction of bounded orbits near the collinear Lagrange points is then summarized.

Finally, the specific reference trajectories used in the orbit determination error analysis and station-keeping studies in this work are introduced.

1. Stability of the Libration Points in the CR3BP

The accomplishments of those researchers who have constructed bounded orbits near collinear libration points are particularly significant because the collinear points are considered "unstable" points of equilibrium but with (only) one mode producing positive exponential growth. Bounded motion in their vicinity, therefore, is determined by deliberately not exciting the unstable mode. A second mode produces negative exponential orbital decay and is also deliberately not excited. In the CR3BP, the remaining four eigenvalues are purely imaginary. The existence of initial conditions that result in only trigonometric (sinusoidal) functions as solutions means that the collinear libration points, while unstable, possess *conditional stability* (with proper choice of initial conditions) in the linear sense.^[18]

The triangular libration points are marginally stable in the linear sense for a specific range of primary mass ratio in the CR3BP. Purely imaginary roots in two conjugate pairs are obtained for $\mu \leq 0.0385$, which is given here to four decimal places and is sometimes referred to as Routh's value.^[19] The mass ratios (listed here to three decimal places), for example, in the three-body systems of the Earth-Moon ($\mu = 1.216 \times 10^{-6}$), Sun-Earth+Moon ($\mu = 3.022 \times 10^{-6}$) and Sun-Jupiter ($\mu = 9.485 \times 10^{-4}$) all satisfy the mass ratio requirement for marginal stability of the triangular points in the linearized model. Natural satellites, such as the Trojan asteroids or a moon of Saturn, occupy linearly stable orbits near triangular libration points in their respective systems.

2. Stability of the Libration Points in the ER3BP

Several researchers have analyzed the stability of the libration points in the elliptic problem, where both the mass ratio, μ , and the primary orbit eccentricity, e , influence stability.^[18-22] The instability of the collinear libration points as determined in the circular problem for all the values of mass parameter persists for the elliptic problem; an analysis of the collinear points shows instability for any combination of the values of both μ and e .

The results of a linearized stability analysis regarding the effects of eccentricity and mass ratio on the linear stability of the triangular points have been published by Danby^[21] and then later by Bennett^[22]. Both Danby and Bennett have numerically generated graphic depictions of the linear stability region in the μ - e plane. For the eccentricity in the Sun-Earth+Moon ER3BP, the value of μ which ensures linear stability is only slightly less than Routh's value (decreased by approximately one percent). An interesting aspect of the μ - e stability region is that a range of values of μ greater than Routh's value also defines a region of linear stability for a specific range of values of e less than .3143.

3. Construction of Bounded Collinear Libration Point Orbits

The initial goal in the process of generating bounded orbits near a collinear (unstable) libration point is to avoid exciting the unstable mode associated with the linearized motion. The meteoric dust particles that may be orbiting near Lagrange point L_2 in the Sun-Earth system could only linger near that point if they arrive with the "correct" initial position and velocity states relative to L_2 . The "correct" initial conditions will only (primarily) excite the stable modes associated with the linearized motion and not (or minimally) excite the unstable mode. The degree to which the unstable mode is excited will determine the length of time that the dust particles linger near L_2 .

The third-order analytic representation is used in this work to provide the initial model for the trajectories. The method of successive approximations, using the linearized solution as the first approximation to the nonlinear orbital path, and the method of dual time scales are used to derive the third-order result.^[6,7,23] The method of successive approximations is used to generate an asymptotic series in an appropriately small parameter. (The square root of the eccentricity of the primary orbit, that is the orbit of the Earth-Moon barycenter about the Sun, is the small parameter used here.) The method of dual time scales is used to convert the system of ordinary differential equations into a system of partial differential equations. In general, the method of multiple scales allows the various nonlinear resonance phenomena to be included in the approximate analytic solution and provides a method to remove secular terms. (Here, "secular" refers to terms that include the time variable and is derived from the French "siècle" meaning century.)

The analytic solution of Richardson and Cary^[7] for the Sun-Earth+Moon ER3BP has been derived to fourth order, but the third-order approximation is found to be sufficient for this research.^[9-14] A numerical integration algorithm, using a differential corrections procedure that is designed to adjust the first guess as obtained from the analytic approximation, can then be used to numerically generate the orbit of interest. A method developed by Howell and Pernicka^[9-14] is used here to generate the orbital paths. Their method initially employs the approximate analytic solution to compute target points. A two-level (position matching then velocity matching), multi-step differential corrections algorithm is used to construct a numerically integrated, bounded trajectory that is continuous in position and velocity. A solar radiation pressure model developed by Bell^[16] is also incorporated in the numerical integration procedure.

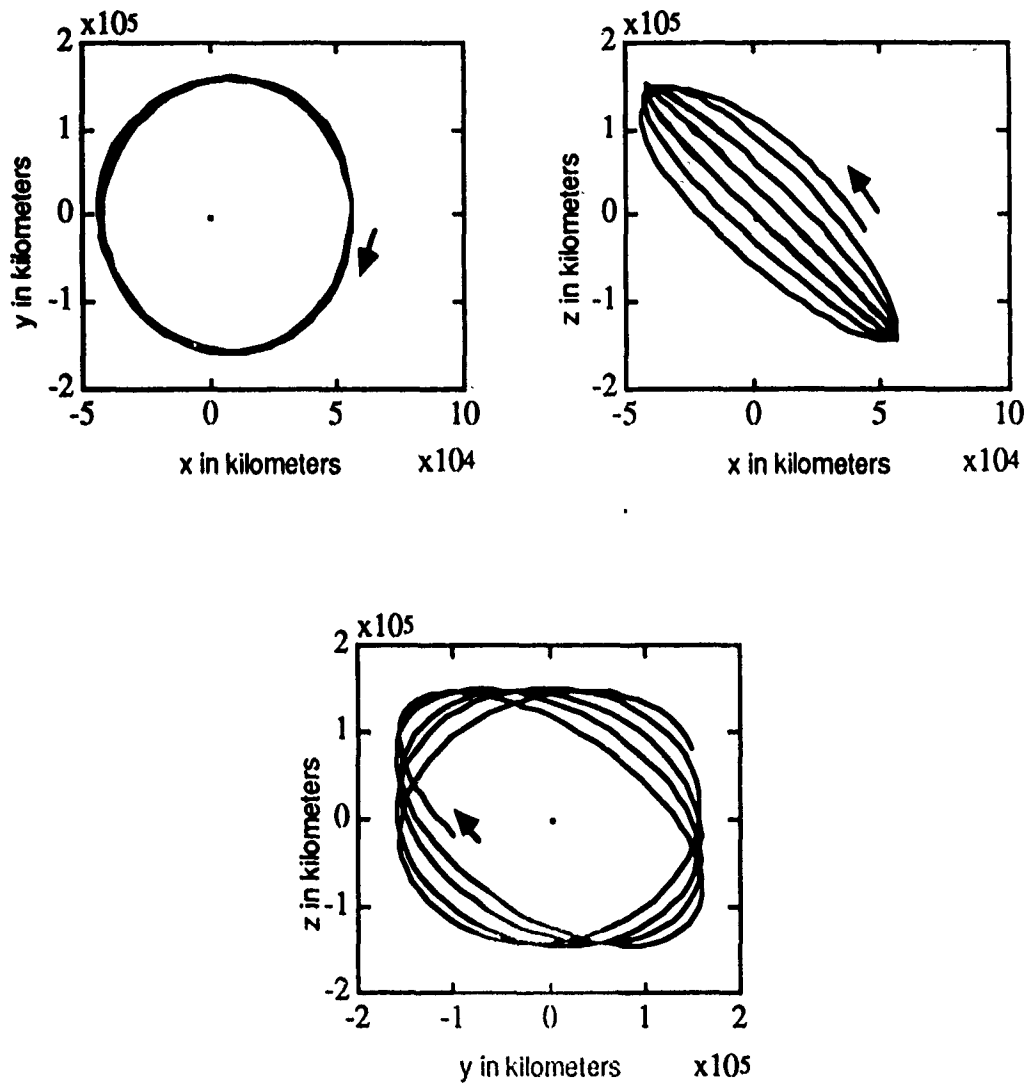
The method of Howell and Pernicka, including solar radiation pressure, uses an initial analytic guess that represents a halo orbit or, alternatively, a considerably smaller Lissajous path. The higher-order terms tend to slightly alter the first-order periodic or quasi-periodic path. Consequently, the initial target path for a halo orbit will generally not be precisely periodic. The two-level,

multi-step differential corrections procedure then adjusts the initial analytic target orbit and, therefore, will compute a halo-type orbit that is nearly (but not exactly) periodic.

4. The Reference Paths Generated for This Work

Precisely periodic halo orbits exist in the CR3BP. They also exist in the ER3BP, but, in the ER3BP, they are multiple revolution trajectories with periods much longer than those of interest here. Nearly periodic orbits are more practical in the ER3BP and are much more likely to be used in mission planning; therefore, the goal here should be slightly modified to be the comparison of Lissajous and "halo-type" orbits. The general shapes of the three-dimensional halo-type and Lissajous orbits can be seen by plotting three orthographic views of each orbit, using the tabular data from the numerical integration routine. Figure 1-4 depicts three orthographic views of point plots for the Lissajous orbit used in this research. Figure 1-5 contains three orthographic views (on a slightly different scale) of the considerably larger halo-type orbit. (Note that, in general, the amplitude ratio for Lissajous trajectories is arbitrary. In halo orbits, however, constraining the amplitude ratio results in equalized frequencies for in-plane and out-of-plane motion.) The orbits are depicted in the rotating reference frame centered at L_1 .

Both orbits are clearly not periodic; a Lissajous orbit is often called a quasi-periodic path, and these two orbits could clearly be termed quasi-periodic or Lissajous paths. The major difference between the orbits is the larger size of the halo-type orbit; however, other differences are also present. The maximum x and y excursions of the halo-type orbit are approximately four times as large as those of the Lissajous path. Furthermore, the direction of motion (clockwise versus counterclockwise), as viewed in the y-z orthographic depiction, is different for the two orbits used here. The direction of motion on the halo-type orbit is counterclockwise in the y-z depiction; the direction of motion is clockwise in the y-z depiction for the Lissajous path. (Both orbits include clockwise motion in the x-y depiction.)



Indicates the direction of motion.



Indicates the location of the libration point.

Figure 1-4. Three Orthographic Views of a Lissajous Orbit.

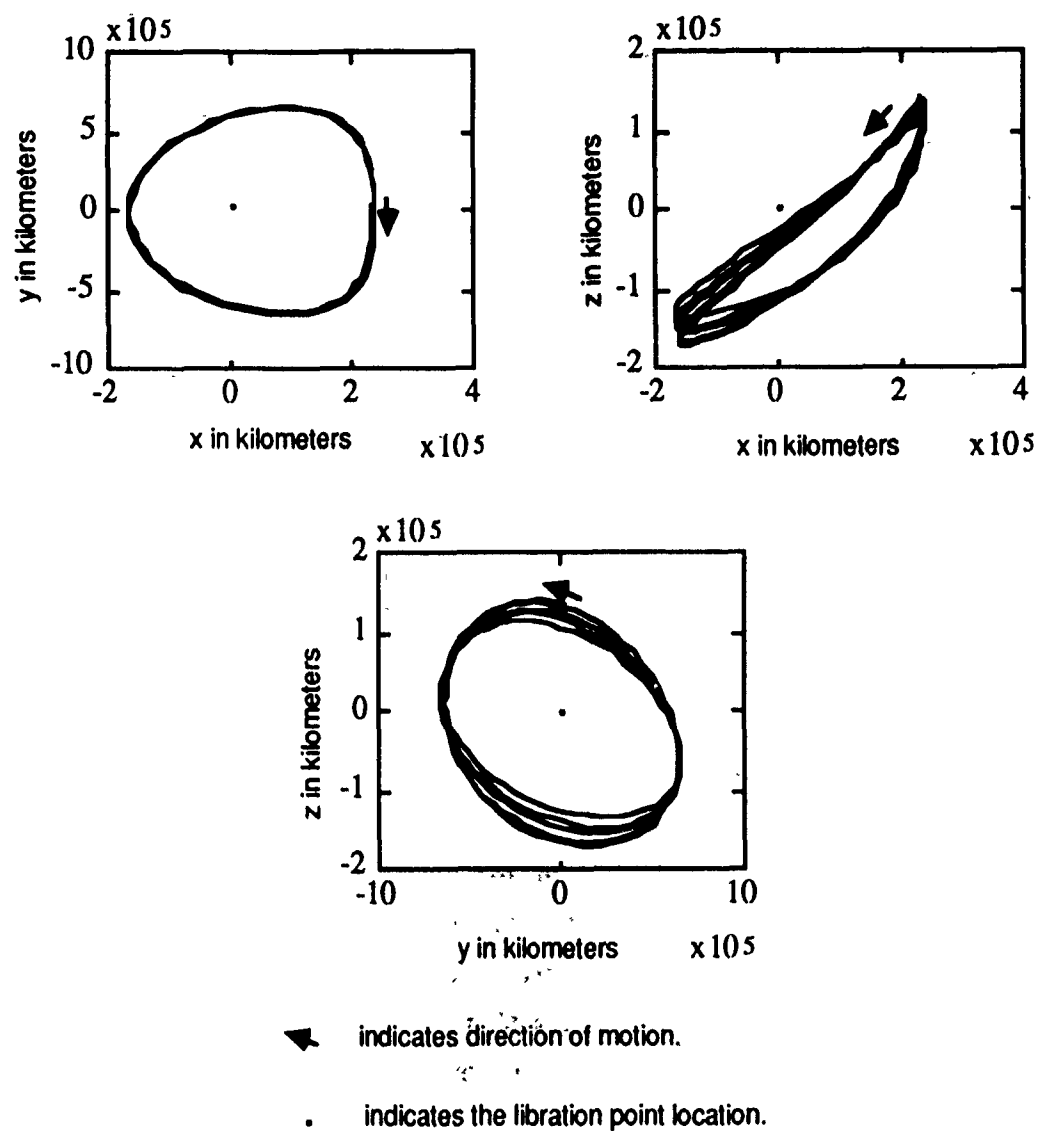


Figure 1-5. Three Orthographic Views of a Halo-Type Orbit.

The two orbits can also be differentiated in terms of the direction of the maximum z excursion in the x-z depiction. If the maximum z excursion is in the positive z direction, the orbit can be termed a member of a "northern family" of orbits. When the maximum z excursion of the orbit is in the negative z direction, the orbit is termed a member of a "southern family" of orbits. In the x-z orthographic depiction, the smaller (Lissajous) path can be seen to be a member of a northern family of orbits, while the halo-type orbit is a member of a southern family of orbits.

Future work with these two orbits will include studies that generally require access to a nominal path that is at least piecewise smooth. Some method of curve fitting the numerically integrated data must consequently be investigated.

5. Curve Fitting the Nominal Path

The primary goal of this work is the completion of orbit determination error analysis for libration point trajectories. The conventional method for solution of state estimation problems, and the technique used in this effort, involves linearizing the nonlinear equations of motion about a reference solution (nominal path) and then applying linear estimation techniques. The orbit determination process is thus changed from estimating the state of a nonlinear system to estimating the linear, time-varying deviations from the reference trajectory.

The reference solution used in this research is generated by numerical integration of the nonlinear equations of motion. In one study, an investigation that used a consistent dynamic model for all comparisons, Richardson^[8] has shown that a slight reduction in fuel expenditure can be realized if a numerically integrated, rather than an approximate analytic, nominal path is computed. The numerical integration method developed by Howell and Pernicka^[9-14] is used here to generate a set of reference points for both position (three states) and velocity (three states), relative to the libration point of interest, at specified times. Time series point plots of all six state

variables for approximately a 2-year segment of a Lissajous orbit are depicted in Figures 1-6 (position states) and 1-7 (velocity states). The method computes numerical data for the six states in a reference frame that is centered at the libration point (in this case L_1) and that rotates with the primaries. However, the state estimation techniques and station-keeping algorithms used in this work require access to a continuous nominal path, rather than point plots, of acceptable accuracy.

The reference trajectory, represented as a (piecewise) smooth curve, could be constructed, approximately or exactly, through the points obtained from the numerical integration routine. The work here assumes that a curve that passes through the numerical data (exactly) is preferred. The effort required to generate a numerical solution, including forces modeled consistent with the ER3BP (or even more accurately modeled with ephemeris data) would seem to be wasted if the reference curve deviates too far from the numerical data. However, a method that approximates a smooth curve through the points is also desirable; that is, linear interpolation between the numerical data points was not considered acceptable. In one study, Pernicka^[9] found that station-keeping costs for a libration point orbit were, in fact, sensitive to the accuracy of the curve fit. Clearly, a piecewise linear curve fit could not accurately match the concavity of the actual orbital path between data points, regardless of the size of the time steps used in the numerical integration routine.

Four methods of generating a curve for the nominal trajectory have been evaluated: Fourier series, least squares, weighted least squares, and cubic splines. The states associated with a quasi-periodic path were thought to be the most difficult to curve fit; therefore, various Lissajous trajectories were used to evaluate the curve-fitting methods. After several curve fitting evaluations, a cubic spline interpolation routine was selected to be used to model the reference trajectory in the state estimation simulations. The comparisons of the curve fit methods are fully described in Gordon.^[15]

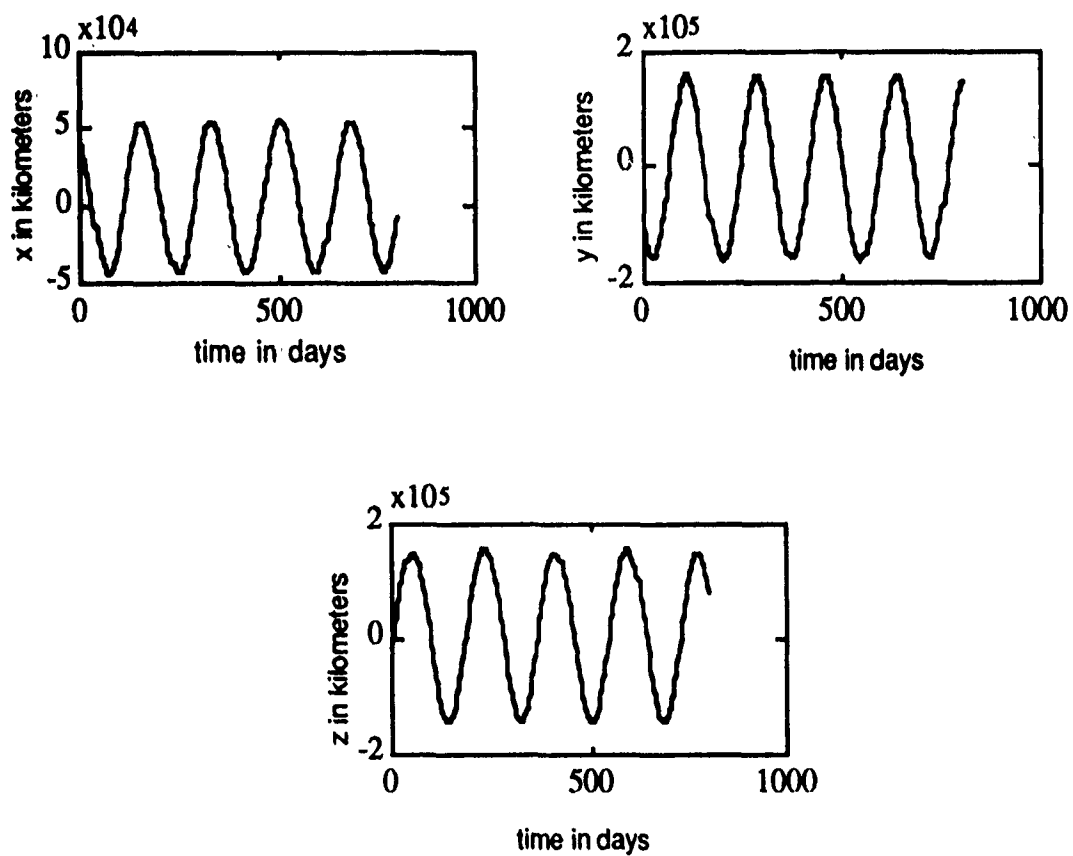


Figure 1-6. Time Series Plots of Three Lissajous Position States.

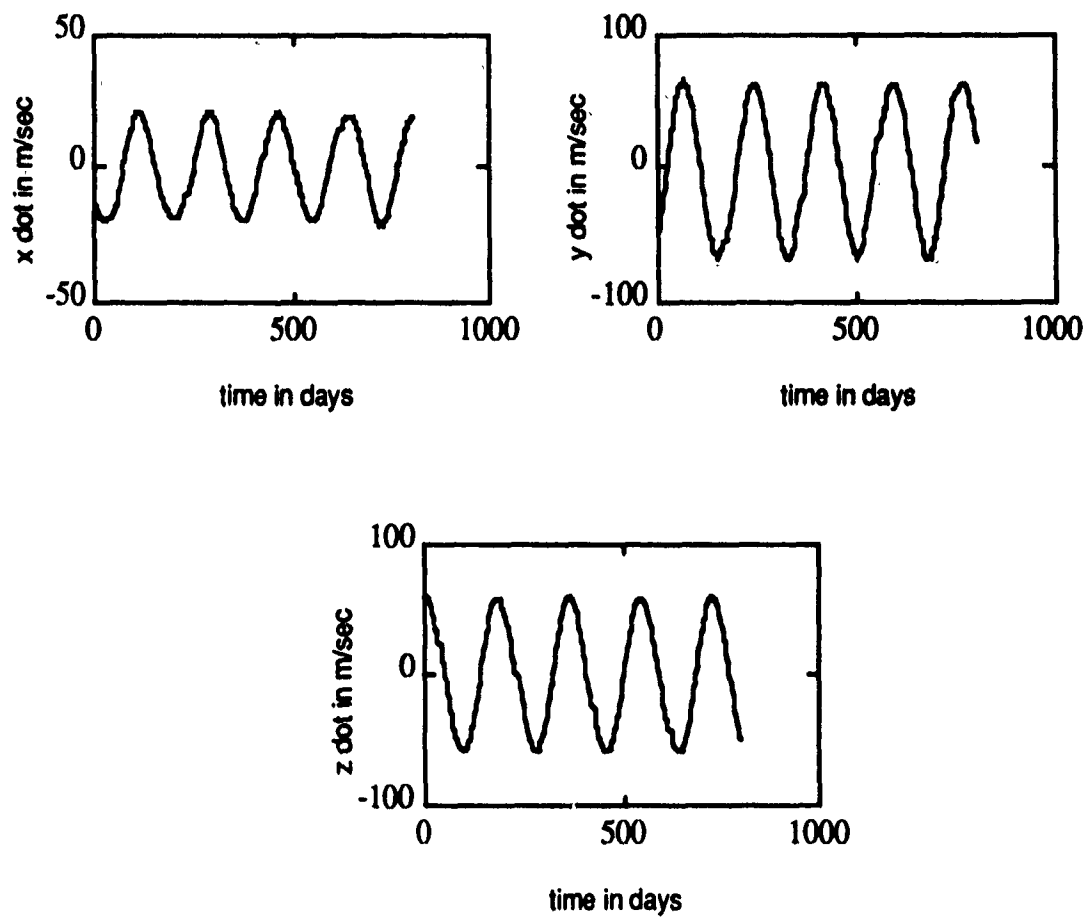


Figure 1-7. Time Series Plots of Three Lissajous Velocity States.

CHAPTER 2: ORBIT DETERMINATION ERROR ANALYSIS

Complete, exact knowledge of the state of a spacecraft in orbit is generally not possible. Individual state variables cannot be measured precisely, and available measurements are usually some function of the state variables. For instance, a spacecraft moving along a libration point trajectory in the Sun-Earth system may be tracked using range and range-rate measurements containing random errors. The spacecraft may be affected by forces not included (or inadequately represented) in the dynamic model, and model parameters may be uncertain. By definition, the linearized system of equations used to model the nonlinear state variations is a further approximation. Also, actual control inputs may vary slightly in magnitude and direction from those commanded. These sources of error make knowledge of the spacecraft state uncertain. Computation of the most likely current state of the spacecraft in the presence of measurement and model uncertainty is the focus of orbit determination.

Error analysis involves an investigation of the impact of various sources of error on orbit determination. The output of an error analysis, as used in this work, provides the magnitudes of state vector variances and covariances, thus quantifying the relative contributions of the significant error sources. This output could then be used to predict how an improvement in measurement accuracy, for instance, would lessen state uncertainty. One benefit of more accurate knowledge of the state might be a reduction in station-keeping costs. A mathematical procedure can be developed to combine all information about the spacecraft state and filter this observed data based on the varying degrees of uncertainty. The filter then produces a "best

estimate" of the state and additionally quantifies the resulting state variable uncertainties in preparation for an error analysis.

The first goal of this research is to investigate orbit determination error analysis for libration point trajectories. The conventional method for solution of state estimation problems, and the technique used in this effort, involves linearizing the nonlinear equations of motion about a reference solution (nominal path) and then applying linear estimation techniques. The orbit determination process is thus changed from estimating the state of a nonlinear system to estimating the linear, time-varying deviations from the reference trajectory. The reference solution used here is generated by numerical integration of the nonlinear equations of motion. The integration routine produces a tabular listing of each of the six state variables, indexed by the time steps used in the numerical computation. The reference path is then modeled by passing a cubic spline, with the independent variable being time, individually through each of the six state variables (three position and three velocity).^[15]

This chapter includes a brief background summary of filtering methods, and the three methods used for error analysis in this work are then discussed. These three methods are the Kalman filter, batch weighted least squares covariance analysis, and consider covariance analysis. Each of these methods computes a covariance matrix at a specified epoch, and the diagonal entries in the covariance matrix are the variances of the state vector elements. The square roots of these six entries are estimates of the state uncertainty levels at the indicated epoch.

The Kalman filter is fully derived in the discussion below for use in both orbit determination and error analysis investigations. The remaining two methods (covariance analysis and consider covariance analysis) are derived only for error analysis, but either method can be used as an important step in the derivation of a batch weighted least squares filter. The following chapter includes a discussion and comparison of the results derived from implementation of these three methods. The state vector variance levels determined from the error analysis studies for both Lissajous and halo orbits can then be used in future station-keeping simulations.

A. BACKGROUND

The historical and mathematical background associated with filtering theory and error analysis originates with least squares theory. The least squares techniques based on the theories of Gauss, Legendre, and Adrain were powerful methods that initially were used to explain the motions of the heavenly bodies. In particular, the development of a sequential algorithm, recursive least squares, by Gauss is fundamental to modern linear filtering theory.^[24] Gauss also selected a weighting scheme for errors that allowed his weighted least squares approach to result in a linear, unbiased, minimum variance estimate.^[25,26] In Great Britain during 1912, Sir Ronald Aylmer Fisher introduced the maximum likelihood method.^[25,27,28] The analysis of variance, as used in error analysis, was also developed chiefly by Fisher, and he introduced the terms "variance" and "analysis of variance."^[29]

In the years surrounding World War II, the driving forces behind the continuing research involving estimation algorithms changed. The original focus was motivated by the need to track objects at low altitudes near the Earth. During World War II, probabilistic methods were recognized to be valuable in addressing problems in radio communications, radar, and anti-aircraft defense.^[30] In the early 1940s, Norbert Wiener, in the United States, and Andrei Nikolaevich Kolmogorov, in the Soviet Union, developed input-output relationships for statistically optimal filters.^[31,27] Both investigated the problem in the frequency domain. Wiener provided optimal estimates only in the steady-state regime for a continuous system, while Kolmogorov also treated the discrete-time problem.^[31] In 1942, the first explicit solutions for least-squares estimates associated with a stochastic process were provided by Wiener using stationary signal and noise processes.^[32] Wiener found that the solution of the Wiener-Hopf integral equation could be used to determine the covariance function of the estimation process. He approached the problem by using Fourier analysis and developed an integral equation for determining the impulse

response matrix for the filter.^[33] However, Wiener-Kolmogorov filters and related follow-on research results had some of the following drawbacks:^[32]

- (1) They were complicated, often requiring the solution of auxiliary differential and algebraic equations and determination of the roots of polynomials.
- (2) They were not easily updated with increases in the observation interval.
- (3) They could not be conveniently adapted to a vector approach.

After World War II, much of the research was redirected to the problem of orbital motion (but now of spacecraft, not planets). With the new focus, implementation required that the filtering methods be adaptable to vectorized models.

In the 1950s and after, research into determination of satellite orbits was a driving force in the development of state space filters. The Apollo program established the need and provided the resources for development and application of optimal filters and also focused the efforts of many in the scientific community.^[30] The frequency domain integral methods of Wiener and Kolmogorov gave way to the methods of least squares adapted to dynamic models that were described by differential equations. J.W. Follin at Johns Hopkins University in 1955 and M. Blum in 1958 developed recursive approaches based on this idea and laid the foundation for the development of dynamic filters.^[27,30] In 1959, Peter Swerling published a method of estimating satellite orbits near Earth from observational data.^[27,30] He developed an innovations process for updating position estimates. Swerling's work was the first known attempt to tackle updates in a vector estimation problem, and his useful recursive formulation can be specialized to obtain the Kalman filter.^[32,27,30]

Rudolf Emil Kalman is usually credited with the development of a state-space, nonstationary, recursive filter that is in wide use today. However, the claim is not universally accepted. Swerling unsuccessfully challenged the editors of the *AIAA Journal* to give him credit for the discovery of the Kalman-type filter.^[27] Swerling's

update equations for the error covariance were in a much more cumbersome form than those produced by Kalman; and Kalman's algorithm, though more restrictive than Swerling's, was particularly suited to the dynamic state estimation problems associated with spaceflight research.^[32] In March 1960, Kalman published his first description of the recursive filter.^[34] In April of 1960, Richard H. Battin independently developed a recursive optimal filter similar to that of Kalman.^[35,36] Then, in November 1960, R.L. Stratonovich independently obtained the Kalman filter equations by treating the linear filter as a special case in nonlinear filtering.^[32,37]

Initially, Kalman derived and published the discrete model of his filter. In 1961, Kalman and Richard S. Bucy published a continuous version of the sequential filter, commonly called the Kalman-Bucy filter.^[30] Research interest in the Kalman filter continued with Stanley F. Schmidt's development of a Kalman filter that could be implemented using an on-board digital computer for guidance in a circumlunar mission.^[30] The linear theory that forms the basis of the Kalman filter could have been a handicap for such mission implementation; however, Schmidt linearized the equations of motion about the nominal path and formulated the filter to update (extend) the nominal path after every position fix. Schmidt first applied this extended filter to the C-5A aircraft navigation system.^[30] Consequently, the extended Kalman filter is sometimes identified as the Kalman-Schmidt filter.

B. The Kalman Filter

Kalman's early published articles^[38,39] were somewhat difficult to understand. When Schmidt^[30] initially tried to apply an operational Kalman filter, he and his engineering staff found it necessary to have initial and follow-up briefings from Kalman. Schmidt found the notation and the concepts used in the filter's development to be difficult to grasp.^[30] Strang^[25] recently suggested that the sections of most texts that include discussions of the Kalman filter are rather discouraging to read. Every author has his or her own

notation; even with similar notation, one Kalman filter can look different from another because authors also have several choices between equivalent equations for propagation of the error covariance and Kalman gain matrices. So, even beyond notational differences, propagation equations may appear to vary in a mathematical development of the Kalman filter.

The Kalman filter is a least squares formulation that incorporates a dynamic model.^[26] For a spacecraft in orbit, the governing dynamic model, that is, the set of equations of motion, is combined with available measurements to improve knowledge of the spacecraft state. The linearized model and the state transition matrix used in the orbit determination investigations have been previously described. The measurement process is added in this section, and the equations are written for the measurement residuals relative to the nominal path. Recall that the nominal path is defined by six cubic splines passing through the numerical data representing the states. Then, the measurement and dynamic models (and the associated notation) used in the following derivation are

$$\text{Measurements: } \tilde{z}_k = M_k \tilde{x}_k + \bar{v}_k \quad (2-1)$$

$$\text{Dynamic Model: } \tilde{x}_{k+1} = \Phi(k+1, k) \tilde{x}_k, \quad (2-2)$$

where \tilde{z}_k is the measurement residual vector at time step k ; \tilde{x}_k is the residual state vector at time step k ; M_k is the measurement matrix that is linearized about the nominal path; $\Phi(k+1, k)$ is the state transition matrix at time step $k+1$ relative to time step k ; and \bar{v}_k is the measurement noise vector and is assumed to have the statistics

$$E(\bar{v}_k) = \bar{0} \quad (2-3)$$

$$E(\bar{v}_k \bar{v}_k^T) = V_k \quad (2-4)$$

where "E" is the expectation operator, $\bar{0}$ is the zero vector, and V_k is the measurement noise covariance matrix. (Process noise is incorporated in this model in a later section; control inputs are not considered in these orbit determination error analysis studies.)

In this work, both range and range-rate tracking are simulated. The measurement matrix, M_k , is linearized about the nominal path represented by six cubic splines passing through the numerical data for the six spacecraft states. The two scalar nonlinear tracking equations are:

$$\text{range} = R = [(x-x_s)^2 + (y-y_s)^2 + (z-z_s)^2]^{1/2} \quad (2-5)$$

$$\text{range-rate} = \dot{R} = [(x-x_s)(\dot{x}-\dot{x}_s) + (y-y_s)(\dot{y}-\dot{y}_s) + (z-z_s)(\dot{z}-\dot{z}_s)]/R. \quad (2-6)$$

Here, the subscript "s" denotes the coordinates associated with the tracking station. The measurement matrix, M , is a time-varying matrix, derived from equations (2-5) and (2-6) through a linearizing process, and is written

$$M = \begin{bmatrix} m_{11} & m_{12} & m_{13} & 0 & 0 & 0 \\ m_{21} & m_{22} & m_{23} & m_{24} & m_{25} & m_{26} \end{bmatrix}, \quad (2-7)$$

where

$$m_{11} = m_{24} = (x - x_s)/R, \quad (2-8)$$

$$m_{12} = m_{25} = (y - y_s)/R, \quad (2-9)$$

$$m_{13} = m_{26} = (z - z_s)/R, \quad (2-10)$$

$$m_{21} = [(\dot{x} - \dot{x}_s)R^2 - \text{NUM}(x - x_s)]/R^3, \quad (2-11)$$

$$m_{22} = [(\dot{y} - \dot{y}_s)R^2 - \text{NUM}(y - y_s)]/R^3, \quad (2-12)$$

$$m_{23} = [(\dot{z} - \dot{z}_s)R^2 - \text{NUM}(z - z_s)]/R^3, \quad (2-13)$$

$$\text{NUM} = [(x - x_s)(\dot{x} - \dot{x}_s) + (y - y_s)(\dot{y} - \dot{y}_s) + (z - z_s)(\dot{z} - \dot{z}_s)]. \quad (2-14)$$

If M_k represents the matrix M evaluated at time t_k , the time-varying, linearized vector measurement equation at time t_k is then given by

$$\tilde{z}_k = \begin{bmatrix} \tilde{z}_1 \\ \tilde{z}_2 \end{bmatrix} = \begin{bmatrix} \tilde{R} \\ \dot{\tilde{R}} \end{bmatrix} = M_k \tilde{x}_k + \bar{v}_k \quad (2-15)$$

for residuals from the nominal path. The time-varying measurement matrix, M_k , has the nonzero entries (2-8) through (2-13) that are evaluated along the nominal path. The measurement residual vector, \tilde{z}_k , represents measured deviations from the nominal path. The vector \tilde{v}_k , as the measurement noise vector, indicates that the updates have some level of uncertainty.

A measurement that arrives at step k and the system propagation equation that provides an estimate of the state at step k can be combined using weighted least squares. (See Gordon^[15] for a complete discussion of the least squares and weighted least squares approaches.) The system equation can be propagated to step k from the "best" estimate of position at step $k-1$ using the state transition matrix. One key to determining how to weigh (filter) these two estimates (the measurement and the state propagated from previously filtered measurements) is to use the covariance matrix in a weighted least squares process. The covariance matrix that depends on the measurements through step $k-1$ can be denoted by \hat{P}_{k-1} . The covariance matrix at step k , before the measurement at step k is incorporated, is denoted by \tilde{P}_k . Propagation of the state covariance matrix can be illustrated by first defining \tilde{x}_k as the estimate propagated to state k before measurement \tilde{z}_k , \hat{x}_k as the estimate after measurement \tilde{z}_k , and \tilde{x}_k as the true state propagated to state k .

The propagation equations can then be written

$$\tilde{x}_k = \Phi(k, k-1) \hat{x}_{k-1}, \quad (2-16)$$

$$\tilde{x}_k = \Phi(k, k-1) \tilde{x}_{k-1}, \quad (2-17)$$

$$\hat{P}_{k-1} = E[(\tilde{x}_{k-1} - \hat{x}_{k-1})(\tilde{x}_{k-1} - \hat{x}_{k-1})^T], \quad (2-18)$$

$$\begin{aligned}
\tilde{P}_k &= E[(\tilde{x}_k - \hat{x}_k)(\tilde{x}_k - \hat{x}_k)^T], \\
&= E[(\Phi(k, k-1)\tilde{x}_{k-1} - \Phi(k, k-1)\hat{x}_{k-1})(\Phi(k, k-1)\tilde{x}_{k-1} - \Phi(k, k-1)\hat{x}_{k-1})^T] \\
&= E[\Phi(k, k-1)(\tilde{x}_{k-1} - \hat{x}_{k-1})(\tilde{x}_{k-1} - \hat{x}_{k-1})^T \Phi^T(k, k-1)] \\
&= \Phi(k, k-1) E[(\tilde{x}_{k-1} - \hat{x}_{k-1})(\tilde{x}_{k-1} - \hat{x}_{k-1})^T] \Phi^T(k, k-1). \quad (2-19)
\end{aligned}$$

Hence, using (2-18) in (2-19), an equation for mapping the covariance matrix from state $k-1$ to state k is given by:

$$\tilde{P}_k = \Phi(k, k-1) \tilde{P}_{k-1} \Phi^T(k, k-1). \quad (2-20)$$

The measurement residual vector \tilde{z}_k can be combined with the state estimate at step k in a weighted least squares solution by utilizing additional definitions. For instance, the state uncertainty vector at time t_k is defined as $\bar{\epsilon}_k$ and

$$\tilde{x}_k = \hat{x}_k + \bar{\epsilon}_k \quad (2-21)$$

where the state uncertainty is assumed to have the statistics

$$E(\bar{\epsilon}_k) = \bar{0} \text{ (the zero vector)}, \quad (2-22)$$

$$E((\tilde{x}_k - \hat{x}_k) \bar{v}_k^T) = 0 \text{ (the zero matrix),} \quad (2-23)$$

$$E(\bar{\epsilon}_k \bar{\epsilon}_k^T) = \tilde{P}_k. \quad (2-24)$$

The above definitions can be used to combine the measurement and dynamic models to produce a "best" estimate of the spacecraft state using a weighted least squares approach. Initially, an augmented set of four matrices can be formed; that is, we let

$$\bar{b} = \begin{bmatrix} \tilde{z}_k \\ \tilde{x}_k \end{bmatrix}, \quad (2-25)$$

$$A = \begin{bmatrix} M_k \\ I \end{bmatrix}, \quad (2-26)$$

$$\bar{e} = \begin{bmatrix} \bar{v}_k \\ \bar{\epsilon}_k \end{bmatrix}, \quad (2-27)$$

$$V = \begin{bmatrix} V_k \\ \tilde{P}_k \end{bmatrix}. \quad (2-28)$$

The matrices (2-25), (2-26), and (2-27) can be used to combine equations (2-1) and (2-21) into a matrix equation

$$A \tilde{x}_k + \bar{e} = \bar{b}. \quad (2-29)$$

The weighted least squares formulation for this matrix equation uses the inverse of the matrix V , defined in (2-28), for weighting the errors in an unbiased, minimum variance scheme. Minimizing the cost function $J(\tilde{x})$, where $J(\tilde{x}) = \bar{e}^T V^{-1} \bar{e}$, is completed by substituting (2-29) into the cost function and then setting the first derivative (of the cost function) with respect to \tilde{x} equal to zero. This computation returns the solution for the optimal state estimate \hat{x}_k , which minimizes the cost function $J(\tilde{x})$, at time t_k as

$$\hat{x}_k = (A^T V^{-1} A)^{-1} A^T V^{-1} \bar{b}. \quad (2-30)$$

The equations (2-25) through (2-28) can then be used in equation (2-30) to produce^[41]

$$\hat{x}_k = (M_k^T V_k^{-1} M_k + \tilde{P}_k^{-1})^{-1} (M_k^T V_k^{-1} \tilde{z}_k + \tilde{P}_k^{-1} \tilde{x}_k). \quad (2-31)$$

This solution for \hat{x}_k in (2-31) requires the inversion of a matrix that may be quite large. Kalman developed a sequential algorithm that requires inversion of a smaller matrix at each step. From the definition of the covariance matrix in (2-18) and by then using (2-30)

and (2-29), in that order, the covariance matrix can be represented as

$$\hat{P}_k = (A^T V^{-1} A)^{-1}. \quad (2-32)$$

Using (2-26) and (2-28) in (2-32), a computationally efficient equation for \hat{P} can be derived:

$$\hat{P}_k = (M_k^T V^{-1} M_k + \tilde{P}_k^{-1})^{-1}. \quad (2-33)$$

While the covariance matrix \hat{P}_k is the essential matrix used to complete the error analysis (covariance analysis) portion of this work, the full Kalman filter, including the state vector update equation, is derived here for completeness. The full Kalman filter may also be quite useful as an optimal observer in follow-on research concerning this problem.

The Schurr identity or "inside-out rule" can be used to give a smaller dimension matrix for inversion:

$$\begin{aligned} \hat{P}_k &= (M_k^T V^{-1} M_k + \tilde{P}_k^{-1})^{-1} \\ &= \tilde{P}_k - \tilde{P}_k M_k^T [M_k \tilde{P}_k M_k^T + V_k]^{-1} M_k \tilde{P}_k. \end{aligned} \quad (2-34)$$

The Kalman gain matrix can be derived from (2-34) as

$$K_k = \tilde{P}_k M_k^T [M_k \tilde{P}_k M_k^T + V_k]^{-1}. \quad (2-35)$$

Using equation (2-35), equation (2-34) can be rewritten as

$$\hat{P}_k = \tilde{P}_k - K_k M_k \tilde{P}_k = [I - K_k M_k] \tilde{P}_k. \quad (2-36)$$

This allows equation (2-31) to be expressed in a more computationally efficient form:

$$\begin{aligned} \hat{x}_k &= [I - K_k M_k] \tilde{P}_k (M_k^T V_k^{-1} \tilde{z}_k + \tilde{P}_k^{-1} \tilde{x}_k) \\ &= [I - K_k M_k] \tilde{x}_k + [I - K_k M_k] \tilde{P}_k M_k^T V_k^{-1} \tilde{z}_k. \end{aligned} \quad (2-37)$$

This expression for \hat{x}_k can be reduced further by showing that

$$[I - K_k M_k] \tilde{P}_k M_k^T V_k^{-1} = K_k, \quad (2-38)$$

so that

$$\hat{x}_k = \tilde{x}_k + K_k [\tilde{z}_k - M_k \tilde{x}_k]. \quad (2-39)$$

The relationships in equations (2-16), (2-20), (2-35), (2-36), and (2-39) can be combined to produce a weighted least squares estimate of the (dynamic) state of the spacecraft relative to the nominal path and in the presence of measurement errors. These five equations are used here to determine the spacecraft residual state at a given epoch. The covariance matrix, \hat{P}_k , reflects the uncertainty associated with a given residual state at the selected time. A final adjustment to the error covariance equations can also ensure that the filter accepts at least a small portion of each measurement residual update.

One problem associated with the filter is divergence; one reason for this divergence can be the filter's failure to accept measurement updates. As in recursive least squares, the filter can "go to sleep" and not accept any substantial part of new measurements. Similarly, in batch least squares, a single observation has a decreasing effect on the solution as the number of observations increases. The Kalman gain matrix, K_k , depends in part on the state covariance matrix, as defined in equation (2-33). The term $M_k^T V_k^{-1} M_k$ will be, at least, positive semi-definite; thus, \hat{P}_k may decrease as measurements continue to arrive, and the gain matrix can be rewritten using equations (2-36) and (2-38) as

$$K_k = \hat{P}_k M_k^T V_k^{-1}. \quad (2-40)$$

Clearly, if \hat{P}_k decreases, then K_k will decrease as well. The measurement updates, $[\tilde{z}_k - M_k \tilde{x}_k]$, in equation (2-39) will be given little weight, and the update equation (2-39) will, in effect, become $\hat{x}_k = \tilde{x}_k$, ignoring measurements. Modeling errors will cause the system to drift from \tilde{x}_k , and measurements to correct the state will not be incorporated. One solution to the divergence problem is incorporation of system error covariance in the Kalman filter.^[26,40,41] This approach is reasonable because the linear model is, in fact, an approximation, and parameter errors and neglected forces add to the system uncertainty. (However, the appropriate magnitude of the added system uncertainty is somewhat unclear and, perhaps, arbitrary.) Adding system noise modifies the equations as follows:

$$\tilde{x}_k = \Phi(k, k-1) \hat{x}_{k-1} + \bar{w}_k \quad (2-41)$$

where \bar{w}_k is the added system noise vector and W_k is the system noise covariance matrix such that

$$E(\bar{w}_k) = \bar{0}$$

$$E(\bar{w}_k \bar{w}_k^T) = W_k. \quad (2-42)$$

The covariance matrix propagation expression (2-20) then appears as

$$\tilde{P}_k = \Phi(k, k-1) \hat{P}_{k-1} \Phi^T(k, k-1) + W_k. \quad (2-43)$$

The magnitudes of the positive entries in W_k determine the relative weight assigned to the predicted position \hat{x}_k as compared to the measurement \tilde{z}_k . The Kalman filter with system uncertainty is then defined in terms of equations (2-16), (2-43) in place of (2-20), (2-35), (2-36), and (2-39).

The Kalman filter can be used independently to perform a preliminary error analysis.^[40] The computation of the state covariance matrix after the measurement update (\hat{P}_k) provides an indication of the accuracy of the state estimate at a specified time step. The filter equations provide a relatively straightforward method of generating the state covariance matrix. When a nominal trajectory is available, the Kalman gain and the state covariance matrices can be precomputed and stored. That is, only the measurement covariance matrix is required for this computation; measurements are not needed to precompute the covariance matrices.

At any time, the diagonal entries in the state covariance matrix are the variances of the individual states, and the off-diagonal elements indicate the cross-correlation between the states. Also, the square root of the sum of the first three diagonal entries of the covariance matrix (a partial trace) is an indicator of the overall uncertainty in the position states. The overall velocity state uncertainty can likewise be investigated. In general, at a specified

epoch, the square roots of the diagonal elements of the covariance matrix are indicators of the consequences of accumulated uncertainties over the tracking period.

Several methods can be used to compare error contributions. The error budget is a listing of individual error sources and the relative contribution of these sources to the total state uncertainty. A sensitivity analysis that uses various levels of measurement accuracy in the computations can, in turn, inform the filter designer of individual error source contributions. A source-by-source sensitivity analysis may be valuable in assessing potential hardware improvements or measurement scheduling changes.^[40] Sensitivity curves are plots of changes in the uncertainty of an individual state or group of states as measurement accuracy levels are varied. Other useful graphical output includes plots of state uncertainty (square roots of the diagonal entries in the state covariance matrix) and plots of elements of the Kalman gain matrix as functions of time. Both types of plots are depicted later in the results section of this chapter. With added system noise, these plots will appear to approach non-zero steady-state values; thus, the gains do not approach zero, and the filter does not "go to sleep."

C. Batch Weighted Least Squares

Error analysis using batch weighted least squares is similar in many ways to that of the Kalman filter. The algorithm for computation of the covariance matrix in batch weighted least squares is derived here, and much of the notation and derivation, as used in this work, is in common with the Kalman filter. Equations (2-1) through (2-33) from the previously-described Kalman filter formulation are also used (in a similar sequence) in the derivation of batch weighted least squares, and these equations are not repeated here.

The error analysis using batch weighted least squares is developed here as a covariance analysis. (The derivation of state vector updates is straightforward, but is not necessary in this work.) For this error analysis, the diagonal entries of the covariance matrix after a

predetermined, but variable, number of measurement updates can be used to predict state uncertainty levels used in the station-keeping simulations of chapter three.

The differences between the Kalman and batch weighted least squares filters are predominantly in the combination, or filtering, of position updates. In the Kalman filter formulation, measurements and the propagated state estimate are combined in a recursive weighted least squares algorithm, using covariance matrices to determine relative weights. The updated state estimate is then propagated forward, and the process of combining measurements with state estimates is continued until the end of the tracking period is reached. Alternatively, in batch weighted least squares, numerous measurement observations are treated as a batch of position updates that are reduced to a single epoch and combined with the predicted state vector. Here, that epoch is denoted, arbitrarily, as t_0 .

In order to facilitate a simple example, we suppose that two measurements, one at time t_1 and one at time t_2 , need to be combined with the dynamic model's position prediction at time t_0 . Using equations (2-25), (2-26), and (2-29) with the error vector \bar{e} omitted for simplicity, the following matrix equation can be formulated:

$$\bar{b} = \begin{bmatrix} \tilde{z}_1 \\ \tilde{z}_2 \\ \tilde{x}_0 \end{bmatrix} = \begin{bmatrix} M_1 \tilde{x}_1 \\ M_2 \tilde{x}_2 \\ \tilde{x}_0 \end{bmatrix} = \begin{bmatrix} M_1 \Phi(t_1, t_0) \tilde{x}_0 \\ M_2 \Phi(t_2, t_0) \tilde{x}_0 \\ \tilde{x}_0 \end{bmatrix} = \begin{bmatrix} M_1 \Phi(t_1, t_0) \\ M_2 \Phi(t_2, t_0) \\ I \end{bmatrix} \tilde{x}_0 = A \tilde{x}_0. \quad (2-44)$$

In general, many more than two observations will be combined to form the covariance matrix $(A^T V^{-1} A)^{-1}$. For just the two observations in the example above,

$$V = \begin{bmatrix} V_1 & & \\ & V_2 & \\ & & \tilde{P}_0 \end{bmatrix}. \quad (2-45)$$

For this example, the matrix V is dimension 10×10 . The measurement noise matrices V_1 and V_2 are each dimension 2×2 , corresponding to uncertainties in the range and range-rate measurements, and the state covariance matrix \tilde{P}_0 is of dimension 6×6 . A reasonable tracking schedule of 9 range and range-rate measurements per day for 20 days would generate a matrix V of dimension 366×366 . Inversion of the matrix V in the covariance computation $(A^T V^{-1} A)^{-1}$ could then lead to ill-conditioning and associated computational difficulties. In one study for ISEE-3, the error analysis simulations using batch least squares did encounter such numerical difficulties. ^[42]

An adjustment to the weighted batch least squares algorithm that permits inversion of a smaller dimension matrix after each measurement update could reduce possible numerical difficulties. The matrix elements in the covariance matrix $(A^T V^{-1} A)^{-1}$ can be multiplied using definitions (2-44) and (2-45) to give

$$\hat{P}_0^{-1} = \tilde{P}_0^{-1} + \Phi^T(t_1, t_0) M_1^T V_1^{-1} M_1 \Phi(t_1, t_0) + \Phi^T(t_2, t_0) M_2^T V_2^{-1} M_2 \Phi(t_2, t_0). \quad (2-46)$$

The computation can be generalized to k measurements taken after time t_0 to give an equation that can be used for calculation of the state covariance matrix \hat{P}_0 at epoch t_0 :

$$\hat{P}_0^{-1} = \tilde{P}_0^{-1} + \sum_{i=1}^k \Phi^T(t_i, t_0) M_i^T V_i^{-1} M_i \Phi(t_i, t_0). \quad (2-47)$$

The state covariance can then be propagated from t_0 to t_k by using equation (2-20) to give:

$$\hat{P}_k = \Phi(t_k, t_0) \hat{P}_0 \Phi^T(t_k, t_0). \quad (2-48)$$

The propagation equation (2-48) incorporates the assumption that the most recent measurement update arrived at t_k , and thus \hat{P}_k is computed rather than \tilde{P}_k . The diagonal entries of this covariance matrix are the variances of the states at time t_k , after measurement updates through time t_k . Notice that only measurements and the initial state vector (by using the covariance matrix \tilde{P}_0) are considered uncertain in this formulation. The results of covariance matrix computations for the Kalman filter and for batch weighted least squares will be compared using identical tracking schedules and statistics in the last section of this chapter. However, a third method of covariance matrix calculation that incorporates additional sources of error is first derived.

D. Consider Covariance Analysis

Consider covariance analysis uses a batch weighted least squares formulation but also includes parameter uncertainty.^[41] Model parameters that are considered uncertain in this work are the planetary masses (through the dimensionless mass parameter μ), the locations of the tracking stations, and the solar reflectivity constant. This derivation has some formulas in common with the Kalman filter and with batch weighted least squares covariance analysis; however, the consider covariance matrix derivation is somewhat more complicated than both of these previously described methods. So, a brief overview, including a few general steps in the problem, is provided here, before the full derivation is completed.

The goal of a covariance analysis, as used in this work, is to compute the covariance matrix after some period of tracking. The state uncertainties are described by the magnitudes of the variances found on

the diagonal of this covariance matrix. In general, at the epoch of interest, the state uncertainty is thought to be the consequence of the accumulated uncertainties in the model and the measurements. Some parameters may also be considered uncertain.

The covariance matrix of interest is assumed to be the aposteriori (after measurements through time t_k) covariance matrix \hat{P}_k at epoch t_k . This matrix is defined in equation (2-18) as

$$\hat{P}_k = E[(\hat{x}_k - \tilde{x}_k)(\hat{x}_k - \tilde{x}_k)^T].$$

The state vector denoted by \tilde{x}_k is the true (yet unknown) state; the state vector denoted by \hat{x}_k is the "best" estimate of the true state at time t_k . Here the word "best" means that the vector \hat{x}_k might be computed, for instance, by minimizing a given cost function appropriate to the problem at hand. The covariance matrix \hat{P}_k may be computed recursively, as in the Kalman filter, or in a batch formulation, as in batch least squares. The batch formulation is used here, where the measurements are reduced to an initial epoch and then propagated by using the transition matrices. The addition of uncertain parameters complicates the dynamic and measurement models and, consequently, the computation and propagation of the covariance matrix \hat{P}_k .

The dynamic model is now written^[41]

$$\dot{\tilde{x}} = A \tilde{x} + B \tilde{c}, \quad (2-49)$$

where the matrices A and B are computed from the usual linearizing process relative to the nominal path and by using nominal values for all parameters considered uncertain. The vector \tilde{c} represents the residuals of the parameters considered uncertain relative to predetermined nominal values. Here,

$$\tilde{c} = [\tilde{k} \ \tilde{\mu} \ \tilde{x}_s \ \tilde{y}_s \ \tilde{z}_s]^T, \quad (2-50)$$

where "k" is the dimensionless solar reflectivity constant, " μ " is the dimensionless mass parameter, and " x_s, y_s, z_s " are the scaled tracking station coordinates. The matrix B is time varying and is given by

$$B = \begin{bmatrix} 0 & 0 & 0 & 0 & 0 \\ 0 & 0 & 0 & 0 & 0 \\ 0 & 0 & 0 & 0 & 0 \\ b_{41} & b_{42} & 0 & 0 & 0 \\ b_{51} & b_{52} & 0 & 0 & 0 \\ b_{61} & b_{62} & 0 & 0 & 0 \end{bmatrix}, \quad (2-51)$$

where

$$b_{41} = \frac{s(x+R\mu)}{d^3}, \quad (2-52)$$

$$b_{51} = \frac{sy}{d^3}, \quad (2-53)$$

$$b_{61} = \frac{sz}{d^3}, \quad (2-54)$$

$$b_{42} = \frac{(x+R\mu)-R(1-\mu)+skR}{d^3} - \frac{\mu R+x-R(1-\mu)}{r^3} + \frac{3(1-\mu)(x+R\mu)^2 R - 3sk(x+\mu R)^2 R}{d^5} + \frac{3R\mu(x-R(1-\mu))^2}{r^5}, \quad (2-55)$$

$$b_{52} = \frac{y}{d^3} - \frac{y}{r^3} + \frac{3(1-\mu)(x+R\mu)yR - 3sk(x+\mu R)yR}{d^5} + \frac{3R\mu(x-R(1-\mu))y}{r^5}, \quad (2-56)$$

$$b_{62} = \frac{z}{d^3} - \frac{z}{r^3} + \frac{3(1-\mu)(x+R\mu)zR - 3sk(x+\mu R)zR}{d^5} + \frac{3R\mu(x-R(1-\mu))z}{r^5}. \quad (2-57)$$

The statistics associated with both \tilde{x} (the true state vector) and \tilde{c} (the vector whose elements are the true parameter values) can now be described. The error vector (sometimes called the state uncertainty vector) at time t_k is defined, as in the Kalman filter and batch least squares derivations, as $\bar{\epsilon}_k$ and

$$\tilde{x}_k = \tilde{x}_k + \bar{\epsilon}_k \quad (2-58)$$

where the state uncertainty is assumed to have the statistics

$$E(\bar{\epsilon}_k) = \bar{0} \quad (2-59)$$

$$E(\bar{\epsilon}_k \bar{\epsilon}_k^T) = \tilde{P}_k. \quad (2-60)$$

The consider parameter error vector at time t_k is defined as $\bar{\beta}_k$, and

$$\tilde{c}_k = \tilde{c}_k + \bar{\beta}_k, \quad (2-61)$$

with the consider parameter uncertainty assumed to have the statistics

$$E(\bar{\beta}_k) = \bar{0}, \quad (2-62)$$

$$E(\bar{\beta}_k \bar{\epsilon}_k^T) = 0 \text{ (the zero matrix)}, \quad (2-63)$$

$$E(\bar{\beta}_k \bar{\beta}_k^T) = \tilde{P}_k^c = \tilde{P}_c. \quad (2-64)$$

The matrix $\tilde{\tilde{P}}_c$ is the consider parameter covariance matrix and is assumed in this work to be stationary.

The observation equation for time t_k is now given as

$$\tilde{z}_k = M_k^x \tilde{x}_k + M_k^c \tilde{c}_k + \tilde{v}_k. \quad (2-65)$$

The matrix M_k^x is equal to the matrix M_k described in the Kalman filter derivation; for the computation of M_k^x , the consider parameters are assumed to be at their nominal values. The matrix M_k^c is derived, also by linearizing the nonlinear measurement equations, while assuming that the consider parameters vary about their nominal values and that the state variables are equal to their nominal values. Both matrices are time varying. This matrix is given by

$$M_k^c = - \begin{bmatrix} 0 & 0 & m_{11} & m_{12} & m_{13} \\ 0 & 0 & m_{21} & m_{22} & m_{23} \end{bmatrix}, \quad (2-66)$$

where the six nonzero elements of M_k^c are equal in magnitude but opposite in sign to the indicated elements of M_k^x . For example, the 1,3 entry in the matrix M_k^c is equal, as indicated in equation (2-66), to $-m_{11}$. The statistics associated with the measurement equation are

$$E(\tilde{v}_k) = \tilde{0}, \quad (2-67)$$

$$E(\tilde{\epsilon}_k \tilde{v}_k^T) = 0, \quad (2-68)$$

$$E(\tilde{\beta}_k \tilde{v}_k^T) = 0, \quad (2-69)$$

$$E(\tilde{v}_k \tilde{v}_k^T) = \tilde{V}_k = \tilde{V}. \quad (2-70)$$

In the remaining steps of this derivation, the initial time is assumed to be t_k . (Recall that, in the batch weighted least squares derivation, t_0 was chosen as the initial epoch--the choice is completely arbitrary in the derivation and t_k was chosen here to broaden the presentation.) Therefore, observations, in addition to \tilde{z}_k , can be made at t_{k+1} and t_{k+2} , for example, and these take the form:

$$\tilde{z}_{k+1} = M_{k+1}^x \tilde{x}_{k+1} + M_{k+1}^c \tilde{c}_{k+1} + \bar{v}_{k+1}, \quad (2-71)$$

$$\tilde{z}_{k+2} = M_{k+2}^x \tilde{x}_{k+2} + M_{k+2}^c \tilde{c}_{k+2} + \bar{v}_{k+2}. \quad (2-72)$$

As in batch weighted least squares, these observations (through t_{k+j} , for instance) can be reduced to a specific epoch, such as t_k . However, with consider covariance analysis, the uncertain parameters also have a transition matrix Θ , and a state propagation equation such as equation (2-2) cannot be used. The state propagation now includes the effects of variations in the consider parameters, and the state propagation equation is given by^[41]

$$\tilde{x}(t_{k+1}) = \Phi(t_{k+1}, t_k) \tilde{x}_k + \Theta(t_{k+1}, t_k) \tilde{c}_k, \quad (2-73)$$

$$\dot{\Phi}(t_{k+1}, t_k) = A(t) \Phi(t_{k+1}, t_k) \quad (2-74)$$

with

$$\Phi(t_k, t_k) = I,$$

and

$$\dot{\Theta}(t_{k+1}, t_k) = A(t) \Theta(t_{k+1}, t_k) + B(t) \quad (2-75)$$

with

$$\Theta(t_k, t_k) = 0,$$

where 0 denotes the zero matrix (here it is 6x5). In this work, we assume that the parameter uncertainty does not vary with time; therefore, $\tilde{c}_k = \tilde{c}$. The observations for the k, k+1, k+2, etc time steps can then be combined to give

$$\tilde{z} = M_x \tilde{x} + M_c \tilde{c} + \bar{v}, \quad (2-76)$$

where

$$M_x = \begin{bmatrix} M_k^x \\ M_{k+1}^x \Phi(t_{k+1}, t_k) \\ M_{k+2}^x \Phi(t_{k+2}, t_k) \\ \vdots \\ \vdots \end{bmatrix} \quad (2-77)$$

$$M_c = \begin{bmatrix} M_k^c \\ M_{k+1}^x \Theta(t_{k+1}, t_k) + M_{k+1}^c \\ M_{k+2}^x \Theta(t_{k+2}, t_k) + M_{k+2}^c \\ \vdots \\ \vdots \end{bmatrix}. \quad (2-78)$$

The consider covariance matrix \hat{P}_c , after a predetermined number of measurement updates, can be computed by using the equation (as in weighted or unweighted least squares)

$$\hat{P}_c = \hat{P}_k^c = E[(\hat{x}_k - \tilde{x}_k)(\hat{x}_k - \tilde{x}_k)^T]. \quad (2-79)$$

Before deriving a solution for (2-79) in terms of measurement and model (including parameter) uncertainties, a brief overview of the remaining computational process is included. This consider covariance matrix, \hat{P}_k^c , is the covariance matrix that contains the consequences of model (including parameter) and tracking uncertainty over the specified tracking period, for example from t_k through t_{k+j} . In order to compute this covariance, the measurements over the tracking period of, perhaps, 20 days are reduced to the initial epoch of t_k by using equations (2-77) and (2-78). The matrix \hat{P}_k^c will then be computed and propagated to the end of the tracking period, which is denoted here as t_{k+j} . The propagated covariance matrix \hat{P}_{k+j}^c contains the state variances along the diagonal. The positive square roots of these variances will be the state vector element uncertainties (standard deviations), as computed in this error analysis study.

The optimal residual state estimate \hat{x}_k is required in (2-79) and is computed through a weighted least squares approach; however, when some parameters are considered uncertain, a more complicated derivation of \hat{x} (and thus \hat{P}_c) needs to be addressed. As in the Kalman filter and batch least squares derivations, the cost function $J(\tilde{x}) = \bar{e}^T V^{-1} \bar{e}$ is minimized to find the optimal state estimate \hat{x} . The vector \bar{e} is defined as in (2-27); however, the expanded cost function will now also include consider parameter terms:

$$J(\tilde{x}) = (\tilde{z} - M_x \tilde{x} - M_c \tilde{c})^T V^{-1} (\tilde{z} - M_x \tilde{x} - M_c \tilde{c}) + (\tilde{x} - \hat{x})^T \tilde{P}^{-1} (\tilde{x} - \hat{x}). \quad (2-80)$$

After setting the first derivative of (2-80) equal to zero and after some algebraic simplification, a formula for $\hat{\tilde{x}}$ (an optimal estimate for \tilde{x}) is obtained: [41]

$$\hat{\tilde{x}} = (M_x^T V^{-1} M_x + \tilde{P}^{-1})^{-1} (M_x^T V^{-1} (\tilde{z}_k - M_c \tilde{c}) + \tilde{P}^{-1} \tilde{x}). \quad (2-81)$$

Clearly, a batch or recursive algorithm, using a reformulation of (2-81), could be developed. This algorithm could then be used to predict the "best" estimate of the spacecraft state, where the propagated state (\tilde{x}) and the measurement (\tilde{z}) are appropriately weighted by using the inverses of the covariance matrices \tilde{P} and V , respectively. However, the focus of this research is orbit determination error analysis, and only the aposteriori covariance matrix must be computed to complete this analysis. Optimal state estimates need not be computed. For convenience, we simplify the notation by letting

$$\hat{P} = (M_x^T V^{-1} M_x + \tilde{P}^{-1})^{-1}. \quad (2-82)$$

Notice that \hat{P} is identical to the covariance matrix derived in the batch weighted least squares filter. The adjusted observation equation

$$\tilde{z}_k = M_x \tilde{x} + M_c \tilde{c} + \tilde{v} \quad (2-83)$$

includes the assumption of uncertainty in \tilde{c} . This assumption is valid because the consider parameter errors are assumed to be zero-mean, as depicted in equation (2-59); hence, $E(\tilde{\tilde{c}}) = E(\tilde{c})$. Equation (2-83) is then substituted into (2-81), and, by also using definition (2-82),

equation (2-81) simplifies to

$$\hat{\mathbf{x}} = \hat{\mathbf{P}}(\mathbf{M}_x^T \mathbf{V}_k^{-1} \mathbf{M}_x) \tilde{\mathbf{x}} + \hat{\mathbf{P}}(\mathbf{M}_x^T \mathbf{V}_k^{-1})(\mathbf{M}_c \bar{\boldsymbol{\beta}} + \bar{\mathbf{v}}) + \hat{\mathbf{P}} \tilde{\mathbf{P}}^{-1} \tilde{\mathbf{x}}, \quad (2-84)$$

where equation (2-61) is also used in the simplification. In preparation for computation of the a posteriori covariance matrix $\hat{\mathbf{P}}_c$, the term $(\hat{\mathbf{x}} - \tilde{\mathbf{x}})$ can be found in a compact form as

$$\hat{\mathbf{x}} - \tilde{\mathbf{x}} = \hat{\mathbf{P}} \tilde{\mathbf{P}}^{-1} \bar{\mathbf{e}} + \hat{\mathbf{P}}(\mathbf{M}_x^T \mathbf{V}_k^{-1})(\mathbf{M}_c \bar{\boldsymbol{\beta}} + \bar{\mathbf{v}}). \quad (2-85)$$

Equation (2-85) is computed by using a form of (2-82) given by

$$\tilde{\mathbf{P}}^{-1} = (\hat{\mathbf{P}}^{-1} - \mathbf{M}_x^T \mathbf{V}_k^{-1} \mathbf{M}_x), \quad (2-86)$$

and by also using equation (2-58). After using equations (2-85), (2-70), and (2-64) in definition (2-79) and after some algebra, a compact equation for $\hat{\mathbf{P}}_c$ is derived:^[56]

$$\hat{\mathbf{P}}_c = \hat{\mathbf{P}} + \hat{\mathbf{P}} \mathbf{M}_x^T \mathbf{V}_k^{-1} \mathbf{M}_c \tilde{\mathbf{P}} \mathbf{M}_c^T \mathbf{V}_k^{-1} \mathbf{M}_x \hat{\mathbf{P}} = \hat{\mathbf{P}}_k^c. \quad (2-87)$$

This is the state consider covariance matrix at time t_k , the epoch to which the measurements, compiled within the tracking period, are reduced. Clearly, the consider covariance matrix in equation (2-87) computes a covariance matrix at least as large as the covariance matrix ($\hat{\mathbf{P}}$) computed in batch weighted least squares because the added term $(\hat{\mathbf{P}} \mathbf{M}_x^T \mathbf{V}_k^{-1} \mathbf{M}_c \tilde{\mathbf{P}} \mathbf{M}_c^T \mathbf{V}_k^{-1} \mathbf{M}_x \hat{\mathbf{P}})$ is at least positive semi-definite. As in batch

weighted least squares, this covariance matrix must be propagated from

some initial epoch to a time corresponding to the end of the tracking period. The end of the tracking period is selected here to be t_{k+j} . The existence of the consider transition matrix complicates the covariance propagation equation, where⁽⁴¹⁾

$$\tilde{x}_{k+j} - \tilde{\hat{x}}_{k+j} = \Phi(t_{k+j}, t_k)(\tilde{x}_k - \hat{x}_k) + \Theta(t_{k+j}, t_k)(\tilde{c} - \hat{c}), \quad (2-88)$$

$$\tilde{P}_{k+j}^c = E[(\tilde{x}_{k+j} - \tilde{\hat{x}}_{k+j})(\tilde{x}_{k+j} - \tilde{\hat{x}}_{k+j})^T]. \quad (2-89)$$

If the uncertain parameters were not considered, equation (2-89) could be simply computed by using a form of propagation equation (2-19). However, with parameter uncertainty, expression (2-88) is substituted into equation (2-89), and the following propagation formula for the state covariance (after some algebra) results:

$$\begin{aligned} \tilde{P}_{k+j}^c &= \Phi(t_{k+j}, t_k) \hat{P}_k^c \Phi^T(t_{k+j}, t_k) + \Theta(t_{k+j}, t_k) \tilde{P}_k^c \Theta^T(t_{k+j}, t_k) + \\ &\quad \Phi(t_{k+j}, t_k) \tilde{P}_k M_x^T V^{-1} M_c \tilde{P}_k^c \Theta^T(t_{k+j}, t_k) + \\ &\quad \Theta(t_{k+j}, t_k) \tilde{P}_k^c M_c^T V^{-1} M_x \tilde{P}_k \Phi^T(t_{k+j}, t_k). \end{aligned} \quad (2-90)$$

The covariance matrix \tilde{P}_{k+j}^c can also be denoted here as \hat{P}_{k+j}^c because measurements are assumed to be taken through time t_{k+j} . This a posteriori covariance matrix, propagated to time t_{k+j} , contains the state variances along its diagonal. These variances are the consequences of the measurement, parameter, and force uncertainties that have accumulated over the tracking period from t_k until t_{k+j} . The

positive square roots of these variances can then be used as the state uncertainties (state standard deviations). The results of this error analysis, or more specifically, of this consider covariance analysis, as compared with the previous two methods used in this work for error analysis, will be summarized in the next chapter.

CHAPTER 3: ORBIT DETERMINATION ERROR ANALYSIS RESULTS

How do the results incorporating the error analysis methods covered in this chapter compare to results found in other, similar efforts? This question will be addressed shortly, but first a survey of the input error levels used in similar error analysis studies serves as a valuable introduction. It is noted that these initial uncertainty levels--for instance, measurement, parameter, and force uncertainties--differ, sometimes significantly, in magnitude, but they have been used in several orbit determination error analysis investigations. The values of these uncertainties may be used to compute the diagonal entries in the input covariance matrices (such as V , \tilde{P}_c , and \tilde{P}). The investigations included in this first section deal with libration point halo or halo-type orbits near L_1 in the Sun-Earth+Moon three-body system. (Smaller Lissajous orbits are discussed in the comparisons included in the later sections of this chapter.)

In the next three sections, error analysis results that are produced from each of the three methods (Kalman filter, batch weighted least squares, and consider covariance analysis) discussed previously are also presented; additionally, the results corresponding to selection of both halo-type and Lissajous trajectories as nominal orbits are compared. The error analysis results from several other investigations are then compared with the consider covariance results found in this effort. The error levels to be used in the station-keeping simulations of chapter three are then computed. Finally, in the last results section, a Monte Carlo simulation is used to complete statistical hypothesis tests concerning the probability distributions and the population means of the residual state errors. These error levels, with assumed probability distributions and means, can then be used in Monte Carlo simulations of station-keeping algorithms developed in future research.

A. Survey of Input Error Levels Used in Other Research

Table 1 lists the input error levels assumed in other error analysis studies as compared to the levels used in this study. The errors are denoted by the symbols generally used in the derivation sections of this chapter. The dimensionless solar reflectivity constant is k ; the tracking site location uncertainty is S and is input as an equal uncertainty level for each of the site coordinates x_s , y_s , z_s ; range tracking is R ; range-rate tracking is RR ; and the uncertain mass parameters are μ_e for Earth, μ_s for the Sun, and μ_m for the Moon. The last column contains the uncertainty in the dimensionless mass parameter μ that would be "equivalent" to the errors listed for the individual mass parameters. (Recall that $\mu = (\mu_e + \mu_m)/(\mu_s + \mu_e + \mu_m)$ for the three-body system of interest in this work.) The approximate value of σ_μ (the standard deviation of μ) is calculated from extensive (10,000) Monte Carlo trials while assuming the individual mass parameter error levels that are described in each of these studies. It is this value of mass parameter uncertainty (σ_μ) that is used in the formulation of the consider covariance analysis used in this work.

An entry in Table 1 that is "--" means that the study in question did not clearly indicate if an uncertainty of this type was used. The error levels listed for one entry (Longuski^[46]) are computed from currently used mission planning data provided during private conversations with the several technical experts listed for this source in the references section. Some studies^[42-44] also use additional input error sources in their orbit determination error analysis simulations; however, the errors used in this work include those found to be most significant in the literature. Consequently, the error levels identified in Table 1 for this investigation were then input as the standard deviations (squared, as appropriate, for the variances along the diagonals of the measurement and parameter covariance matrices) for the covariance analysis studies summarized in the following sections.

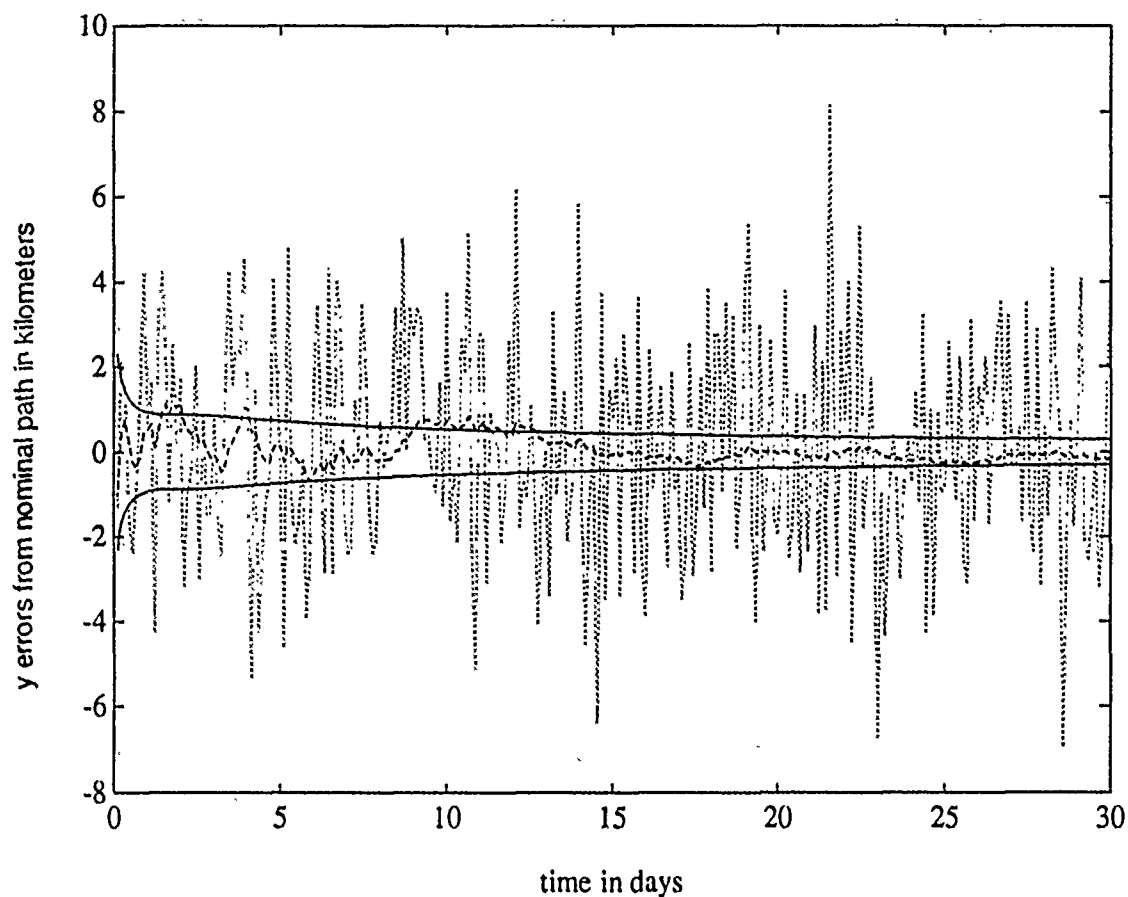
Table 1. Survey of Error Analysis Input Errors.

STUDY	k	ONE STANDARD DEVIATION ERRORS						σ_{μ} ($\times \mu$)
		S (km)	R (km)	RR (m/sec)	μ_e	μ_s ($\leftarrow \text{km}^3/\text{sec}^2 \rightarrow$)	μ_m	
Mistretta ^[42]	15%	--	.010	.007	1.000	3.08 $\times 10^6$.0726	2.335 $\times 10^{-5}$
Joyce ^[43]	10%	.002	.015	.002	.3986	1.327 $\times 10^4$.0490	1.411 $\times 10^{-7}$
Efron ^[44, 46]	10%	.002	.015	.002	3986	1.327 $\times 10^4$.0490	1.411 $\times 10^{-7}$
Rodriguez- Canabal ^[45]	--	.010	.015	.003	--	--	--	--
Longuski ^[46]	13%	.0003	.010	.001	.4903	4030.7	.0100	1.231 $\times 10^{-7}$
This Work	13%	.010	.015	.003	.3986	1.327 $\times 10^4$.0490	1.411 $\times 10^{-7}$

B. Kalman Filter Results

The Kalman filter generates an a posteriori state covariance matrix that can readily be used for error analysis studies. It also computes optimal gain matrices that are used to provide a relative weight to the current measurement versus a prediction of the actual spacecraft position. Therefore, in addition to covariance analysis, the Kalman filter may prove useful as an optimal tracking filter in future research. Its tracking abilities are only partly introduced here for a spacecraft following a nominal halo-type orbit. The results of error analysis using the Kalman filter are then included in the next section, where the results obtained from using the Kalman filter and weighted batch least squares filter covariance analyses are compared.

Results from simulations incorporating the Kalman filter described previously show both good tracking and the anticipated gain propagation characteristics. These characteristics can be depicted in several ways. Figure 3-1 is a plot for the residual $y(t)$ state estimate and is produced from the results of one Monte Carlo simulation that was continued for 30 days. Plots for the other five state variables show similar behavior, but they are not included here. The full state measurement residual vector is corrupted by random noise and is input to the filter. The filter output should "follow" this noisy measurement signal but, at the same time, be consistent with the propagation of the state residual. The positive and negative values of the square root of the (2,2) element of the state covariance matrix, plotted as functions of time, form a one standard deviation envelope for filter uncertainty. This envelope approaches the zero error level because this formulation of the Kalman filter does not use added system noise. These solid (standard deviation) lines appear in Figure 3-1 just above and below the horizontal level that corresponds to zero errors in the residual $y(t)$ state. The line "....." depicts the tracking signal, including errors in the $y(t)$ residual state, that is



Legend:

The upper line "-----" is $+[(\hat{P}_k)_{2,2}]^{1/2}$
 The lower line "-----" is $-[(\hat{P}_k)_{2,2}]^{1/2}$ } These two lines form a one standard deviation envelope around the nominal path

The line "....." is the y state measurement including random tracking errors

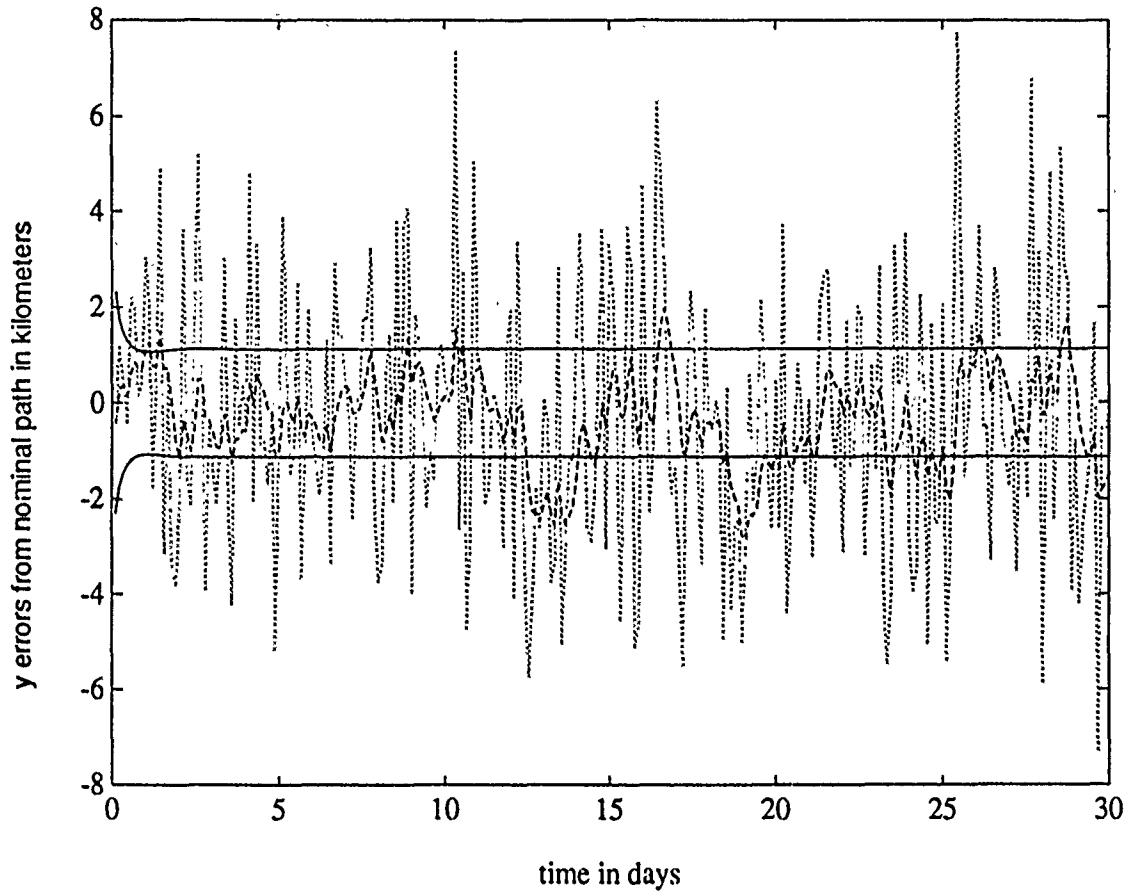
The line "-----" is the y state output from the kalman filter

Figure 3-1. Kalman Filter Plots for the y State Variable.

input for the Monte Carlo run. The dashed line "- - -" is the Kalman filter output. Nine "noisy" measurements are simulated per day, and the filter tends to smooth out tracking uncertainty by continuing to decrease the weighting that the measurements are given in the recursive least squares solution.

The output depicted in Figure 3-1 is from a Kalman filter formulated using equations (2-16), (2-20), (2-35), (2-36), and (2-39). When system uncertainty is not added to the formulation, measurements are given less weight (compared to the propagated state) as the simulation progresses. The lines depicting the standard deviation envelope in Figure 3-1 can be seen to continue to approach the zero-error level, and, as this standard deviation decreases, the measurements can also be seen to have a decreasing effect on the filter output. That is, the filter output can be seen to "smooth out" and approach the zero-error level as measurements continue to arrive. The filter would eventually ignore measurement updates, and this tendency of the Kalman filter is often called "going to sleep." This formulation of the filter (without added system noise) is used in the covariance analysis simulations described in this section because the arbitrary level of added system noise would otherwise affect the covariance analysis; however, to improve the tracking capabilities of the filter, added system noise would be used in a formulation of an optimal tracking filter that could be used in future research.

Figure 3-2 is a plot of the residual $y(t)$ state estimate and is produced from the results of one Monte Carlo simulation of a Kalman filter that includes added system noise in its formulation. The Kalman filter incorporating added system noise uses equations (2-16), (2-35), (2-36), (2-39), and (2-43); the addition of the system noise matrix W_k in equation (2-43) allows both the predicted spacecraft position and the measurement updates to be given continuing, relative weights in the sequential weighted least squares formulation of the Kalman filter. The standard deviation envelope, simulated measurements, and the filter output are depicted in Figure 3-2 with the same characterizations used in Figure 3-1. The one standard deviation envelope in this formulation decreases to a steady-state level within 1 day. The level of added system uncertainty is slightly exaggerated in this example in order to



Legend:

The upper line "—————" is $+\left[\left(\hat{P}_k\right)_{2,2}\right]^{1/2}$
 The lower line "—————" is $-\left[\left(\hat{P}_k\right)_{2,2}\right]^{1/2}$ } These two lines form a one standard deviation envelope around the nominal path
 The line "....." is the y state measurement including random tracking errors
 The line "- - - - -" is the y state output from the kalman filter

Figure 3-2. Kalman Filter Plots for the y State Variable when Added System Noise is Used.

more clearly depict the differences evident in the two types of Kalman filter derivations. The filter output for the y state (" - - - ") tends to "follow" the noisy measurement information (".....") throughout the 30 days of tracking more closely than the filter output presented in Figure 3-1 tends to follow the "noisy" measurements. The addition of system uncertainty, in effect, decreases the relative level of confidence given numerically to the propagated state in the filter and provides a consistent weight in the least squares computation for the measurement updates.

Figures 3-3 and 3-4 show the Kalman gain matrix element (2,2) for two different formulations of the filter. Figure 3-3 depicts the decrease in the gain matrix element for a Kalman filter that does not include added system noise. The magnitude of this entry decreases toward a zero value as measurements continue to arrive in the 30-day tracking period. Note that the gain matrix K_k in equation (2-39) determines the relative weight that measurements are given in the filter update equation; as the gain elements decrease, the filter will tend to more soundly "go to sleep." Figure 3-4 depicts the gain element (2,2) that decreases to a steady-state value after approximately 1 day of tracking. (Recall that the added system noise level in this example is relatively large in order to facilitate illustration of the differences between these two formulations.) The steady-state gain value is nonzero because this Kalman filter derivation incorporates added system noise; a nonzero gain value allows measurements to continue to be given some weight in the filter's state propagation equation. Other gain matrix elements exhibit similar characteristics, but they are not shown here.

The Kalman filter derivation used in this effort for orbit determination error analysis (covariance analysis) incorporates the error sources of initial state uncertainty (the matrix \tilde{P}_0) and measurement noise (the matrix V_k). The addition of system uncertainty (the matrix W_k) improves filter tracking but would not be helpful in completing a covariance analysis. Another method, batch weighted least squares covariance analysis, is similarly derived (to a point) and can be used to possibly confirm the results obtained using the Kalman

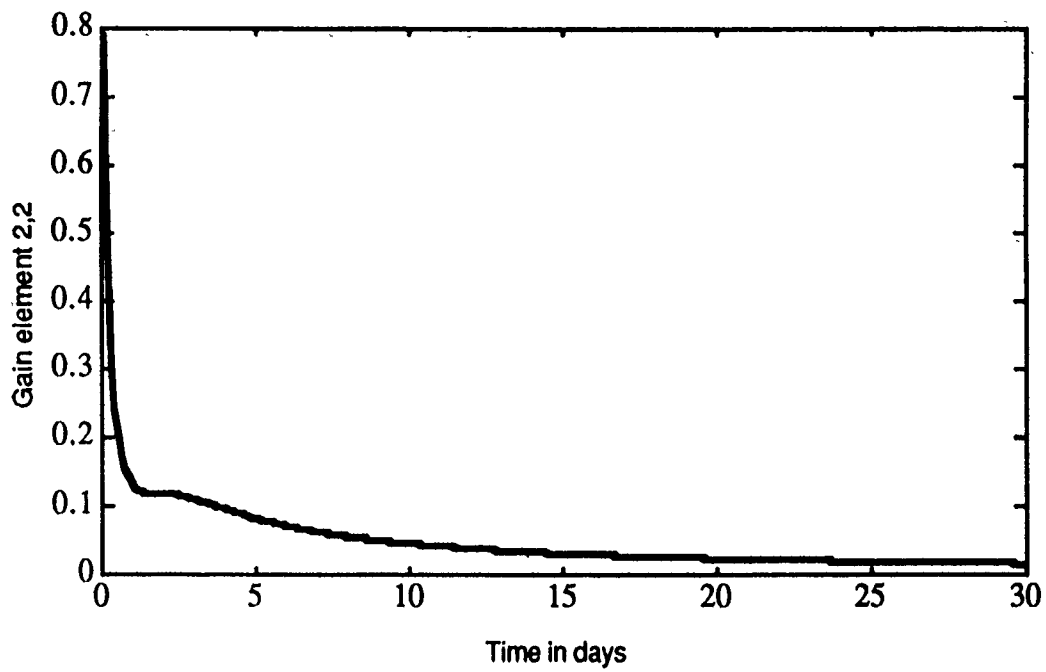


Figure 3-3. Gain Element 2,2

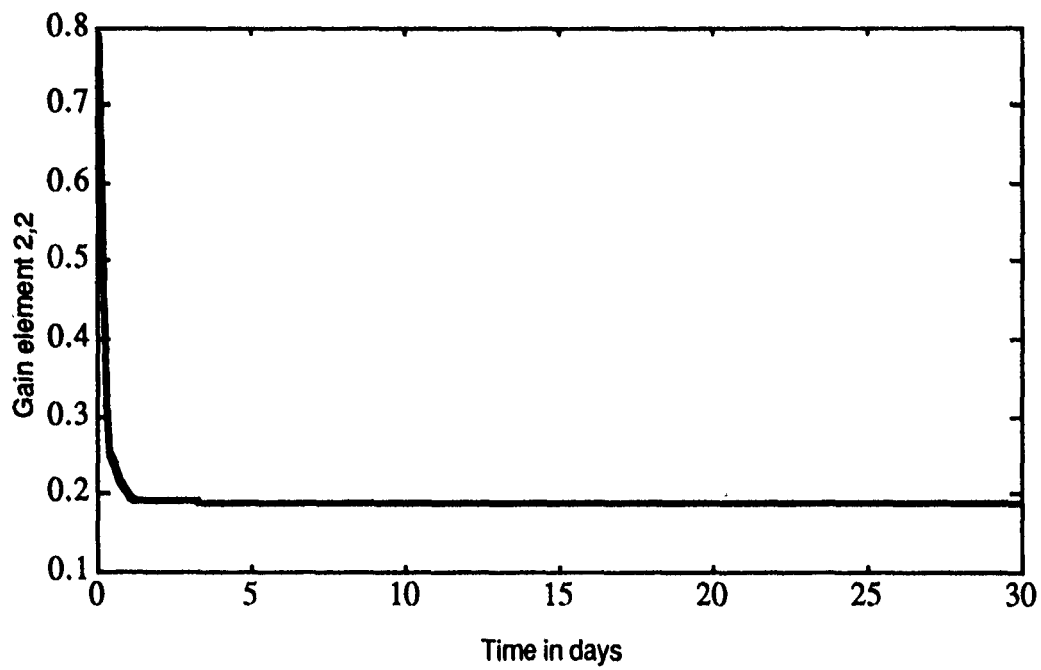


Figure 3-4. Gain Element 2,2 When System Noise is Included in the Filter.

filter. In the following section, the covariance analysis results using a formulation of the Kalman filter that does not include added system noise (uncertainty) is compared to the results obtained from a weighted batch least squares filter.

C. Comparison of Weighted Batch Least Squares and Kalman Filters

The derivations of both the weighted batch least squares and the Kalman filters are somewhat similar. Assuming use of the same level of tracking errors and initial state errors, these two filters should provide the same state vector uncertainty levels after identical tracking periods. (The agreement may be approximate due to numerical round-off error.) The following results, in Table 2, correspond to 180 range and 180 range-rate measurements over a 20-day tracking period for a spacecraft on a nominal halo-type path near L_1 . The standard deviations of the three position states are reduced to one measure of position uncertainty by taking the square root of the sum of the three state (x, y, z) variances. The velocity uncertainty is derived in a similar way.

Table 2. Comparison of Batch Least Squares and Kalman Filters

	<u>Batch Least Squares(B)</u>	<u>Kalman (K)</u>	<u>Percent Deviation (K-B)/K</u>
Range Uncertainty (km)	3.96	4.14	4.35%
Velocity Uncertainty (m/sec)	.00220	.00224	1.82%

Clearly, on the basis of this limited comparison, both methods provide approximately equal estimates of state uncertainty for equivalent input errors and tracking schedules.

It should be noted that the results presented in Table 2 are not due to a single covariance analysis simulation. In fact, all the

results presented for error analysis in this work are averages of several simulations. For example, a covariance analysis could be completed for the first 20 days along the nominal path with $t_0 = 0$ days; an identical 20-day simulation could also be completed along the nominal path with $t_0 = 10$ days. The covariance analysis results from these two runs may be different due to the change in the portion of the nominal path along which the spacecraft is tracked, and average error values based on these two simulations may then be used. The variances (along the diagonals of the covariance matrices) from the two simulations for each of the states are averaged, and this average variance for each of the states can then be considered as the output of the orbit determination error analysis.

Because the covariance analysis results do vary depending on the spacecraft's position in the orbit (and the geometry of the tracking solution), the covariance analysis results presented as part of this effort are actually computed from the averages of 30 simulation runs. Each run generally uses a 20-day tracking period unless otherwise specified, but the initial epoch for each simulation is adjusted (stepped further along the nominal path). The adjustments in the initial epoch are computed so that, after 30 simulation runs are completed, the initial epoch used on the last run has advanced through approximately 180 days (about one "revolution") of the orbit. The positive square roots (the standard deviations) of these "average" variances for the residual states can then be used to represent the state error levels that would eventually be used in a station-keeping simulation.

An interesting area for future research could be the coupling of the orbit determination error analysis and station-keeping as one concurrent simulation; that is, the error analysis could produce a level of residual state uncertainty for the first, say, 20 days of tracking, and the exact (not average) uncertainty could then be input in the Monte Carlo simulation of the station-keeping algorithm. The residual state uncertainty levels derived from the next 20-day tracking period could then, in turn, be input at the 40-day time point as the Monte Carlo simulation continued. In general, orbit determination error analysis and station-keeping simulations are completed

separately; this coupling of the simulations could produce more accurate results in future research.

The next step in this investigation is the addition of parameter errors in the error analysis. With the addition of parameter uncertainty, the comparison of orbit determination error analysis results for both halo-type and Lissajous orbits can be completed using a larger error spectrum. When some parameter errors are assumed to have a nonzero level of uncertainty, the resulting state uncertainty magnitudes for identical tracking schemes may increase compared to the results of the previous two methods (the Kalman and batch weighted least squares filter covariance analyses); consider covariance analysis is a natural method to use when parameter uncertainty is added to this error analysis investigation.

D. Consider Covariance Analysis Results

In the consider covariance analysis studies completed for this work, the initial purpose was to attempt to approximately match the state uncertainty levels derived in other works. The agreement was predicted to be approximate because orbital shapes and sizes and dynamic models are not exactly matched. Also, tracking schedules may not be accurately described for every study. For the research results compared in Table 3, the tracking schedules and the tracking and parameter uncertainty levels were matched as closely as possible. The position uncertainty is computed by taking the square root of the sum of the first three elements along the diagonal of the aposteriori covariance matrix \hat{P}_k . In other words, the total position uncertainty is computed by summing the variances of the x, y, and z states and then taking the square root of this sum. The total velocity uncertainty is computed in a similar way.

The results in Table 3 are arranged in three groups, separated by dotted lines. Within each group, similar tracking schedules and error levels are used when known; the covariances computed in this effort for presentation in Table 3 are average values from 30 simulations. (The input error levels for several error analysis studies were listed in

Table 1.) For instance, the first group includes works by Mistretta^[42] and Heuberger^[47] that pertain to ISEE-3 studies. The study by Mistretta is an error analysis investigation that simulates one range measurement per site per day for 14 days using three tracking sites. It also assumes one range-rate measurement per 10 minutes for the 2 hours that each of the three sites can adequately view the spacecraft. An identical tracking schedule is used in the consider covariance analysis used in this work to attempt to match Mistretta's findings. The study by Heuberger is an analysis of station-keeping costs for ISEE-3, and it uses the error levels represented in Table 3.

In the second and third groupings for the comparisons of Table 3, an attempt is also made to match the tracking schedules and input error levels for which the studies were conducted. In the study by Joyce^[43] for the ISEE-3 mission analysis, a tracking schedule of three range and range-rate measurements per site per day for each of three tracking sites was simulated for 21 days of tracking. In the study by Rodriguez-Canabal^[45], the tracking schedule includes one range measurement per site per day and 8 range-rate measurements per site per day using two tracking sites for 20 days of tracking.

The error levels listed in Table 3 show results that are considered, when allowing for possible force model and nominal path differences, to be in general agreement within groupings; thus, with a significant level of confidence, further simulations are conducted to quantify the state uncertainty levels to be used in the station-keeping simulations of chapter three. (An interesting focus of future research might be to evaluate the differences in station-keeping costs, if any, as a result of using the various orbit determination error levels listed in Table 3. This follow-on research could then also use a statistical "design of experiments" approach to quantify both the sensitivity of the residual state error levels calculated in the error analysis and, in turn, of the station-keeping costs to varying error analysis input uncertainty levels.^[48])

Table 3. Comparison of Consider Covariance Error Analysis Results.

Study	Total Position Uncertainty(km)	Total Velocity Uncertainty(cm/sec)
Mistretta ^[42]	19.81	1.24
This Work	31.25	3.43
Heuberger ^[47]	42.53	3.67
Joyce ^[43]	≤ 10.0	≤ 2.00
This Work	14.98	1.69
Rodriguez- Canabal ^[45]	5.83	0.44
This Work	15.04	1.69

E. Computing Error Levels for Station-Keeping Simulations

Three methods (the Kalman filter, batch least squares, and consider covariance analysis) have now been introduced in this work and can be used to complete an orbit determination error analysis. Of course, other methods of error analysis are also available, but any of these three previously-introduced methods should prove to be useful. The choice between them is generally dependent on the types of errors that need to be included. (It is also partly arbitrary.) For instance, the Kalman filter and batch least squares generate basically equivalent covariance analysis results, given identical inputs such as tracking and initial position error levels. The Kalman filter has the additional benefit of computing current covariance matrices and

position estimates after every measurement update; batch least squares, depending on the specific formulation of the algorithm, can unfortunately exhibit numerical instability^[42] and does not produce state estimates after every measurement update. Alternatively, consider covariance analysis is a weighted batch least squares approach that also incorporates parameter uncertainty; its computation is more complicated, and the contribution of parameter uncertainty tends to accumulate with each measurement update. (See equation (2-87).) In one study^[43] that discussed error analysis for the ISEE-3 mission, parameter uncertainty (specifically solar reflectivity uncertainty) became the dominant error source after just 2 days of tracking and, in fact, caused the state uncertainty to increase as tracking data continued to arrive. Similar behavior was noted in this work when solar reflectivity uncertainty was used as a parameter error source in the consider covariance analysis.

Consider covariance analysis does allow the inclusion of a wide spectrum of uncertain parameters in the batch weighted least squares covariance formulation. When this parameter uncertainty is included in the covariance analysis, the computed residual state error levels increase compared with the levels that result if, for instance, the Kalman filter (derived earlier) would be used in the error analysis. However, the residual state errors resulting from any error analysis study can be used in station-keeping simulations. The tracking updates that are incorporated in the Monte Carlo simulation of the station-keeping algorithm can, in turn, include the residual state uncertainty as one error source.

The size of the residual state errors should have some effect on the station-keeping cost for a spacecraft in a libration point orbit. Several error sources (such as planetary mass, solar reflectivity, and tracking station position uncertainties) have been shown in other studies to be significant contributors to residual state uncertainty, and they should, therefore, be incorporated in the evaluation of station-keeping costs. There are, however, several ways to incorporate these various errors; consider covariance analysis is not the only available approach. The parameter errors can be modeled as random errors in a Monte Carlo simulation of the station-keeping algorithm.

This would allow the orbit determination error analysis simulations to be completed for this effort using only initial position and tracking errors in the batch least squares or Kalman filter covariance analysis. The residual state error levels that are computed in the covariance analysis would undoubtedly then be smaller as the spectrum of parameter errors to be considered is reduced. The method that is eventually used for inclusion of parameter errors somewhere in the station-keeping problem is, in general, dependent on the nature of the problem and the desires of the investigator; however, the method used to model parameter errors (as part of the orbit determination error analysis versus their incorporation as part of the Monte Carlo simulations of the station-keeping algorithm) may have some consistent impact on station-keeping costs and could, therefore, be a fruitful area for future research.

For the current effort, consider covariance analysis is selected as the method to be used to determine the state uncertainty levels that will, in future research, be used in station-keeping studies. The input error levels (except solar reflectivity uncertainty), listed in Table 1 for this work, are used here. Solar reflectivity uncertainty has been used in many of the previous error analysis simulations presented in this effort; however, several studies^[45,49,50] pertaining to future missions involving libration point orbits do not use solar reflectivity uncertainty as an input to an orbit determination error analysis. In fact, these studies use the solar reflectivity uncertainty as a separate random error source in the Monte Carlo simulations of the station-keeping algorithm. (The station-keeping simulations would naturally follow completion of the orbit determination error analysis studies.)

In order to more closely match these recent studies, solar reflectivity uncertainty in this work is also input as an error source in only the station-keeping simulations; however, there is also another reason that solar reflectivity uncertainty is preferred here as an error source in the station-keeping simulations rather than in the orbit determination error analysis. The added parameter uncertainty, especially solar reflectivity, causes the residual state error levels to vary somewhat depending on the spacecraft's position in the orbit.

The 30 covariance analysis trials, completed along the orbit, can still be used to compute average residual state errors; however, the average values will probably not be as "close" to the true residual state error values for a given 20-day segment of the orbit if these values vary widely along the orbit.

Table 4 depicts the range (lowest, highest) of values for the residual state standard deviations resulting from a series of consider covariance analyses. In order to construct this table, a specific value (10%, 5%, 2.5%, or 0%) was selected for the solar reflectivity uncertainty, and a series of 30 consider covariance analyses using 20-day tracking periods were completed. The other parameter uncertainty levels and the tracking schedules are consistent throughout the simulations used to construct the data for Table 4. The first covariance analysis is completed at the "beginning" of the nominal halo-type orbit depicted in Figure 1-5. (Note that Figure 1-5 includes depictions using only the three position states, and the "direction-of-orbit" arrows in this figure are positioned at approximately the orbit start point. The state vector denoting the "beginning" of the orbit includes the three position states and the three velocity states.) Each subsequent covariance analysis is initiated at a position that is approximately 6 days further along track. The halo-type nominal orbit is not perfectly periodic, but it does approximately complete a full revolution in about 180 days. Therefore, this scheme of error analysis simulations will cover approximately one revolution of the nominal halo-type path.

Table 4. Error Analysis Results for a Halo-Type Orbit: Range in the Standard Deviation for Various Levels of Solar Reflectivity Uncertainty.

Coordinate	Minimum, Maximum One Standard Deviation Levels			
	$\sigma_k = 10\%$	$\sigma_k = 5\%$	$\sigma_k = 2.5\%$	$\sigma_k = 0\%$
x (km)	5.24, 27.69	4.20, 17.96	3.32, 9.16	1.38, 1.98
y (km)	3.42, 50.94	2.39, 39.43	2.21, 17.52	1.68, 3.13
z (km)	1.17, 26.87	1.17, 19.03	1.17, 5.69	1.16, 5.18
\dot{x} (cm/sec)	.51, 2.55	.51, 1.74	.32, .81	.10, .36
\dot{y} (cm/sec)	.14, 4.44	.12, 3.59	.09, .98	.08, .22
\dot{z} (cm/sec)	.12, 1.60	.12, 1.25	.11, .60	.11, .28

The contributions of the remaining error sources, other than solar reflectivity uncertainty, were not as noticeably dependent on orbital position. Consequently, solar reflectivity uncertainty is used as a separate error source in the station-keeping simulations discussed in chapter three; it is not used to compute residual state uncertainty levels that are the outputs of an error analysis. The error analysis, completed for later use in the station-keeping simulations, assumes a 20-day tracking arc using 3 passes per day from 3 separate tracking sites. These assumptions closely match those of Joyce.^[43] The input error levels used here were accurately summarized in Table 1. Mass parameter uncertainty will also match the levels found in Joyce. The station position and tracking uncertainty levels will match those used in Rodriques-Canabal.^[45] Solar reflectivity uncertainty can be used in the station-keeping simulations as a random variable. The results of the error analysis simulations are summarized in Table 5. These error levels can be used in the future station-keeping simulations.

Table 5. Error Levels Produced from Error Analysis Studies.

Coordinate	One Standard Deviation Levels	
	Halo-Type Orbit	Lissajous Orbit
x (km)	1.46	1.25
y (km)	2.64	3.35
z (km)	4.81	3.19
\dot{x} (mm/sec)	1.40	1.25
\dot{y} (mm/sec)	1.85	1.41
\dot{z} (mm/sec)	2.49	2.51

Certainly, it is of great interest to compare these error levels with the results of other investigations involving spacecraft in halo (or at least halo-type) orbits near the interior Sun-Earth libration point. Table 6 lists the results of four such error analysis studies that do not include solar reflectivity as an error source.

Table 6. Comparison of Error Analysis Results from Several Sources.

Coordinate	One Standard Deviation Error Levels			
	Rodriguez-Canabal ^[45]	Simó ^[49]	Simó ^[50]	This Work
x (km)	2.7	1.5	1.73	1.46
y (km)	3.9	2.5	2.24	2.64
z (km)	3.4	15.0	5.48	4.81
\dot{x} (mm/sec)	2.4	1.0	1.41	1.40
\dot{y} (mm/sec)	3.5	1.0	1.41	1.85
\dot{z} (mm/sec)	1.3	3.0	2.45	2.49

The error analysis results, computed in this work for use in the station-keeping simulations, agree most closely with the levels computed in Simó^[50]. The agreement can be clearly seen in Table 6. (It should be noted that there are, of course, small differences in the nominal paths and force models used for the works listed in Table 6.)

When all the various input error sources are combined over the 20 days of tracking, the error analysis predicts the levels of state uncertainties listed in Table 5. Technically, these error magnitudes do appear to differ for halo and Lissajous orbits; however, two different Lissajous nominal orbits may show the same variations. Station-keeping costs, determined through simulations using the above error levels, may or may not differ. The testing of the significance of these differences in the error levels will be undertaken in future station-keeping simulations; however, these Monte Carlo simulations will require assumptions about both the type of probability distribution (Gaussian or uniform, for instance) and the mean value of the errors. Therefore, one last area of inquiry in this error analysis study should be concerned with the shape (distribution) and position (means) of the probability distributions for the random errors listed in Table 5.

F. Probability Distribution of the Resulting Errors

Most, if not all, station-keeping studies use random errors as if they were Gaussian with a zero mean. That is, the Monte Carlo simulations associated with the control algorithms use standard deviation levels such as those in Table 5 in a random number generator for which the probability distributions and the mean values of the errors must be assumed. Generally, the uncertainty is assumed to be "white noise"--errors that are zero mean and that tend to closely follow the normal distribution. A covariance analysis is generally a linear algorithm and, in a linear analysis, sums of Gaussian random variables are clearly also Gaussian. In this case, a linear error analysis that then assumes Gaussian, zero mean input errors will, in turn, compute residual state errors that are also zero mean and

Gaussian. However, it is not so clear what distribution the residual state errors might follow if the random errors were alternatively propagated using the nonlinear equations of motion, a method sometimes used in this work.

For this portion of the research, the input error levels listed for this work in Table 1 are assumed, and the nonlinear equations of motion are integrated forward for 20-day arcs. Range and range-rate tracking, station position, mass parameter, and solar radiation pressure random errors were simulated using zero-mean, normally-distributed variables. Numerical integration routines and random number generators available in the software package 386-Matlab^[17] were used in this effort. Three hundred random trials were conducted. Histograms of the resulting errors in position and velocity relative to the nominal orbit for each of the six states are displayed in Figures 3-5 through 3-10. The histograms use ten classes (of equal class width) with midpoints plotted along the horizontal axis.

The vertical axis represents the frequency of responses counted in the classes. These six depictions show distributions of errors that appear to be normally distributed with a mean of approximately zero. (The appearance of a histogram associated with an exactly normally distributed random variable will be discussed at the end of this chapter.) Statistical tests can be conducted to verify these assumptions of the distribution type and location of the mean value.

Initially, it must be determined if the distributions are, indeed, Gaussian. Thus, the hypothesis that the distributions are normal (assumed true) versus the hypothesis that they are not is to be tested. It must be proven to a confidence level of, say, 95%.^[51] Here it is appropriate to use chi-squared (χ^2) goodness of fit tests to test the hypotheses. The goodness of fit test is conducted separately for each of the six coordinates. It compares the observed frequencies (f_i) in the classes used to construct the histograms shown in Figures 3-5 through 3-10 to the expected frequencies (F_i) under the hypothesis that the distribution is normal.

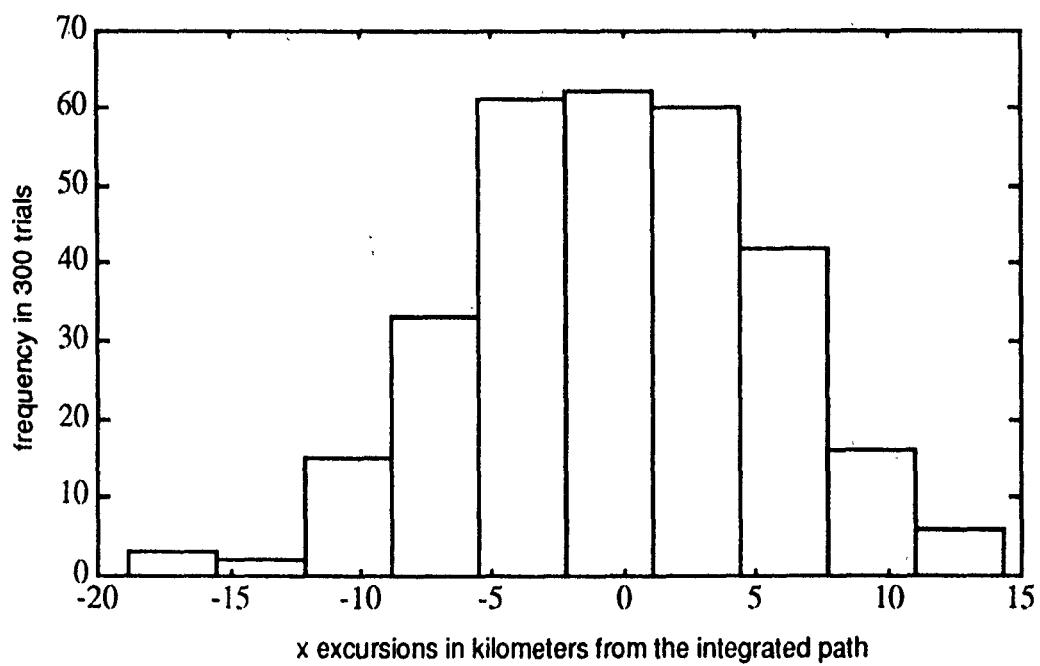


Figure 3-5. Histogram of the x Excursion From the Integrated Path.

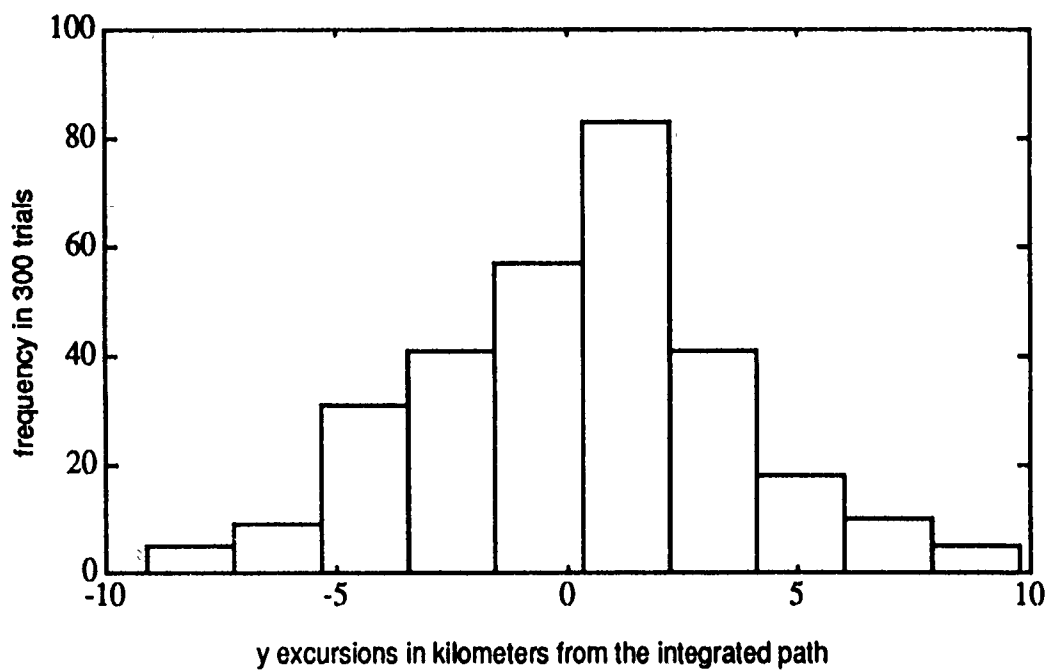


Figure 3-6. Histogram of the y Excursion From the Integrated Path.

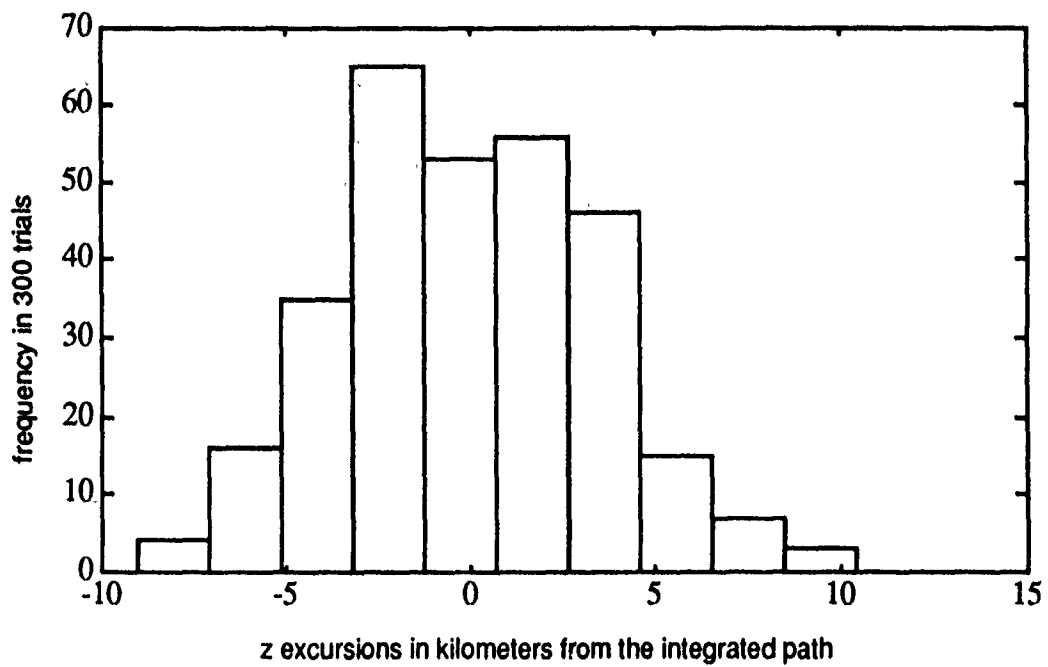


Figure 3-7. Histogram of the z Excursions From the Integrated Path

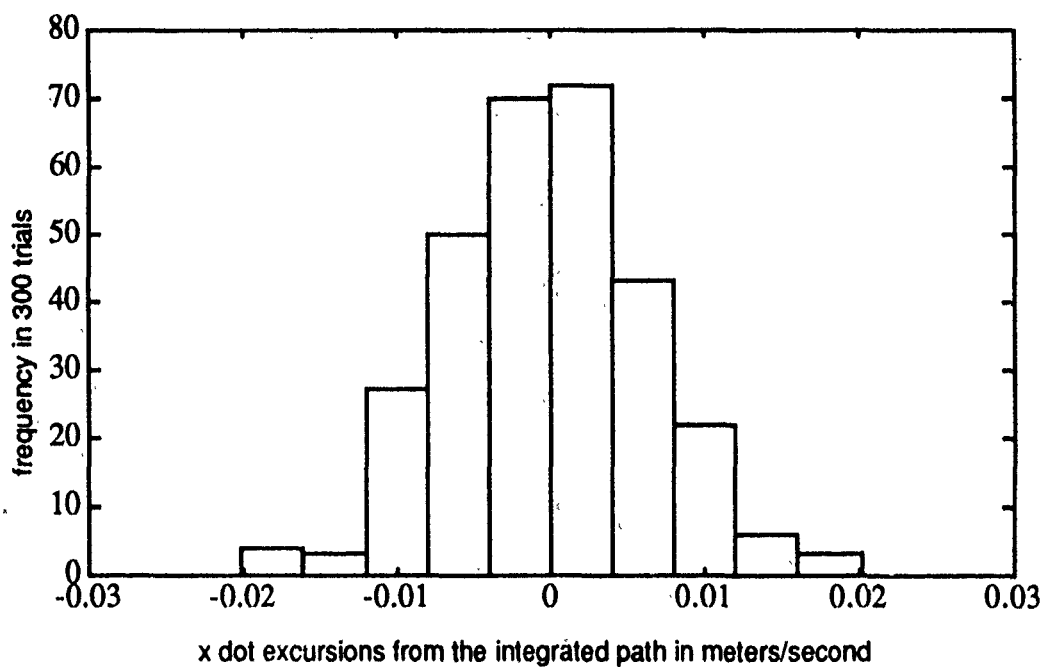


Figure 3-8. Histogram of the x Velocity Excursion From the Integrated Path.

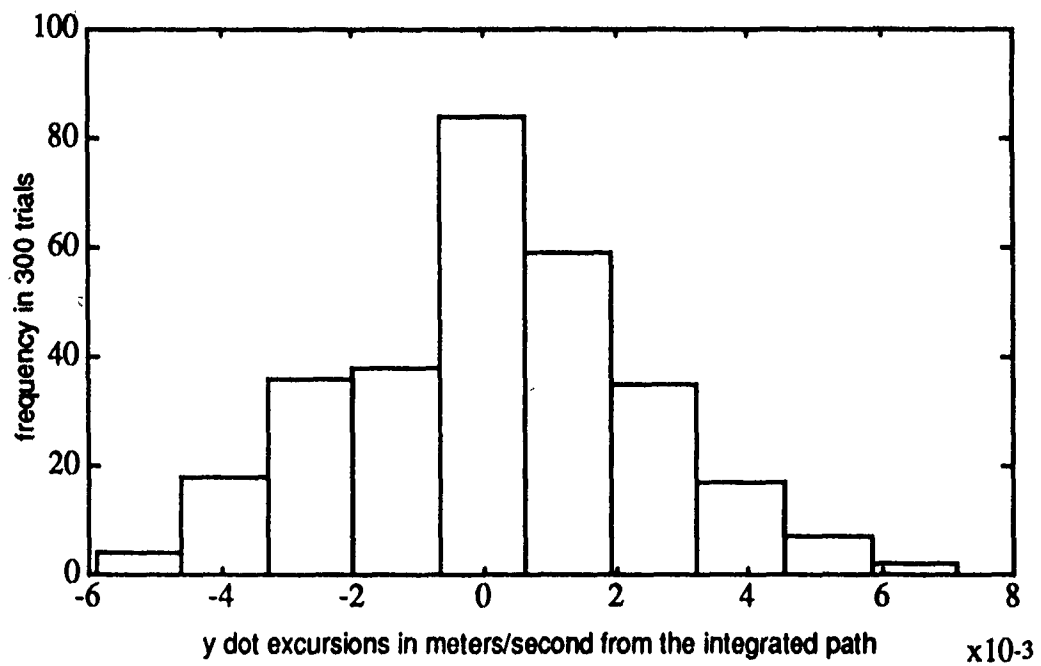


Figure 3-9. Histogram of the y Velocity Excursion From the Integrated Path.

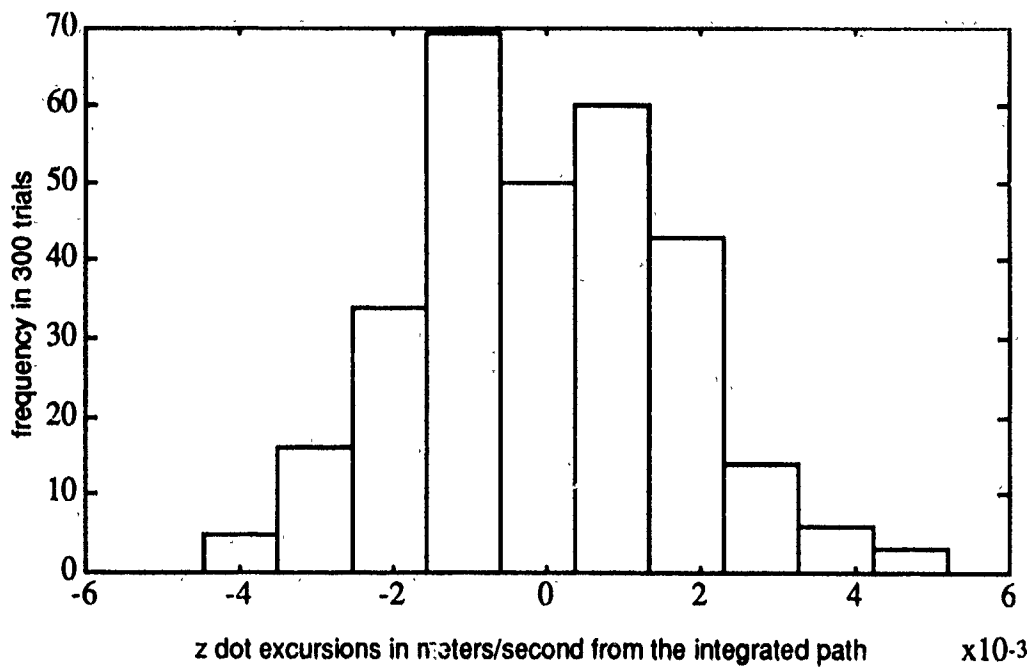


Figure 3-10. Histogram of the z Velocity Excursion From the Integrated Path.

For these tests, the test statistic X^2 is defined

$$X^2 = \sum_{i=1}^k (f_i - F_i)^2 / F_i$$

where k denotes the number of classes in the histogram for each of the six variables. Here, k is ten (or nine if classes must be pooled), and the degrees of freedom for the goodness of fit test are derived from the number of classes. In this investigation, the degrees of freedom for the chi-squared test will be reduced by one because the total of the expected frequencies (f_i) must be equal to the sample size. It is further reduced by two because both the mean and variance used to compute the expected frequencies are computed from the sample data. The χ^2 random variable for these tests then has $k-2-1=7$ (or 6 if pooled) degrees of freedom, a 95% level of confidence, and is equal to 14.07 (or 12.59 if pooling is necessary). This value for χ^2 is found in a table of values for the distribution.^[51]

The hypotheses and the decision rule used for each of the six tests are:

Hypotheses:

H_0 : The Probability Distribution for $(x, y, z, \dot{x}, \dot{y}, \text{ or } \dot{z})$ is normal.

H_1 : The Probability Distribution is not normal.

Decision Rule:

If $X^2 \leq \chi^2$, conclude H_0 .

If $X^2 \geq \chi^2$, conclude H_1 .

The results of these tests are summarized in Table 7 for the Monte Carlo simulation of 300 runs.

Table 7. Results of the Error Analysis Goodness of Fit Tests.

Error	χ^2	χ^2	Conclusion
x	1.712	12.59	H_0 :Gaussian
y	12.486	14.07	H_0 :Gaussian
z	8.524	14.07	H_0 :Gaussian
\dot{x}	5.430	12.59	H_0 :Gaussian
\dot{y}	12.338	12.59	H_0 :Gaussian
\dot{z}	9.725	12.59	H_0 :Gaussian

The general conclusion of this hypothesis test is that the residual state errors that result from the error analysis can be appropriately modeled as Gaussian. Hence, the state errors used in the Monte Carlo simulations of the station-keeping algorithms can be modeled as normally distributed random variables. (It should be noted that the results of the chi-squared goodness of fit test can be presented in different ways, and, in fact, other types of goodness of fit tests are also available. For instance, the well-known Statistical Analysis Software from the SAS Institute uses a Shapiro/Wilk test for normality and, when the same residual state error data is used as inputs to this software, the program indicates that each of the errors is strongly Gaussian with a mean of zero.)

It must also be determined if these normally distributed state errors are also zero-mean. Now the hypothesis to be tested is that the population means for the random errors are zero. This hypothesis is tested six independent times--once for each state variable. The population means are denoted as $\mu_x, \mu_y, \mu_z, \mu_{\dot{x}}, \mu_{\dot{y}}, \mu_{\dot{z}}$, and the conduct of the hypothesis tests assumes that these population means are zero unless proven otherwise. For this statistical test, the standard normal distribution (Z) is the assumed working distribution. The statistical test statistic is denoted by Z^* and is calculated by (using the residual state x as a specific example):

$$Z^* = \frac{\text{sample mean}}{\text{standard error of the mean}} = \frac{\bar{x}}{s\{\bar{x}\}} = \frac{\bar{x}}{s\{x\}/(n^{1/2})}$$

where $s\{x\}$ is the standard deviation of the random variable in question (which is x here) and n is the random sample size. Here, n is 300 random trials. The level of confidence used for this test is again 95%, but here the risk (5%) is divided into both tails of the distribution. Therefore, $Z = 1.960$, which can be found in a table of values for the standard normal distribution.^[51]

The alternatives and decision rule are then:

Hypotheses:

$$H_0: \mu_x = 0.$$

$$H_1: \mu_x \neq 0.$$

Decision Rule:

If $|Z^*| \leq Z$, conclude H_0 .

If $|Z^*| \geq Z$, conclude H_1 .

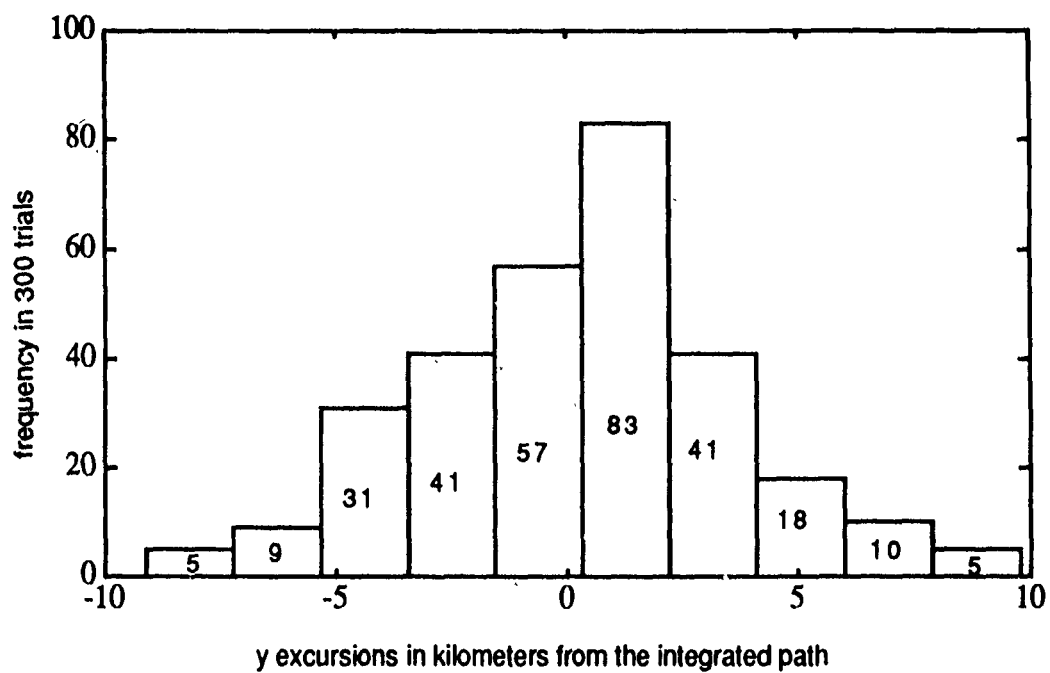
The results are summarized below in Table 8.

Table 8. Hypothesis Test for Zero Error Means.

Error	<u>-Z</u>	<u>Z*</u>	<u>Z</u>	Conclusion
x	-1.960	-1.051	1.960	$H_0: \mu_x = 0.$
y	-1.960	1.193	1.960	$H_0: \mu_y = 0.$
z	-1.960	-.403	1.960	$H_0: \mu_z = 0.$
\dot{x}	-1.960	-.679	1.960	$H_0: \mu_{\dot{x}} = 0.$
\dot{y}	-1.960	1.084	1.960	$H_0: \mu_{\dot{y}} = 0.$
\dot{z}	-1.960	-.518	1.960	$H_0: \mu_{\dot{z}} = 0.$

It may be somewhat interesting to discuss the differences between a distribution that appears to be Gaussian and one that is, in fact, Gaussian. The most appropriate way to present this comparison is through two histograms, one for a variable tested in the discussion above and one for a Gaussian distribution with an identical mean and standard deviation. (The shape of a Gaussian distribution is determined by its standard deviation; the location of the distribution on the real number line is determined by the mean.) The residual y state variable in both the goodness of fit test and the hypothesis test for a mean of zero provided the results that were "closest to causing rejection" and could thus be considered to depart most from the Gaussian distribution. The mean of y is .156635 and the standard deviation of y is 3.34769 in both histograms of Figures 3-11 and 3-12. The histogram in Figure 3-11 is for the actual residual y state, and the observed frequencies f_i are included in each class; the histogram in Figure 3-12 is of a truly Gaussian distribution, and the expected frequencies F_i are included in each class.

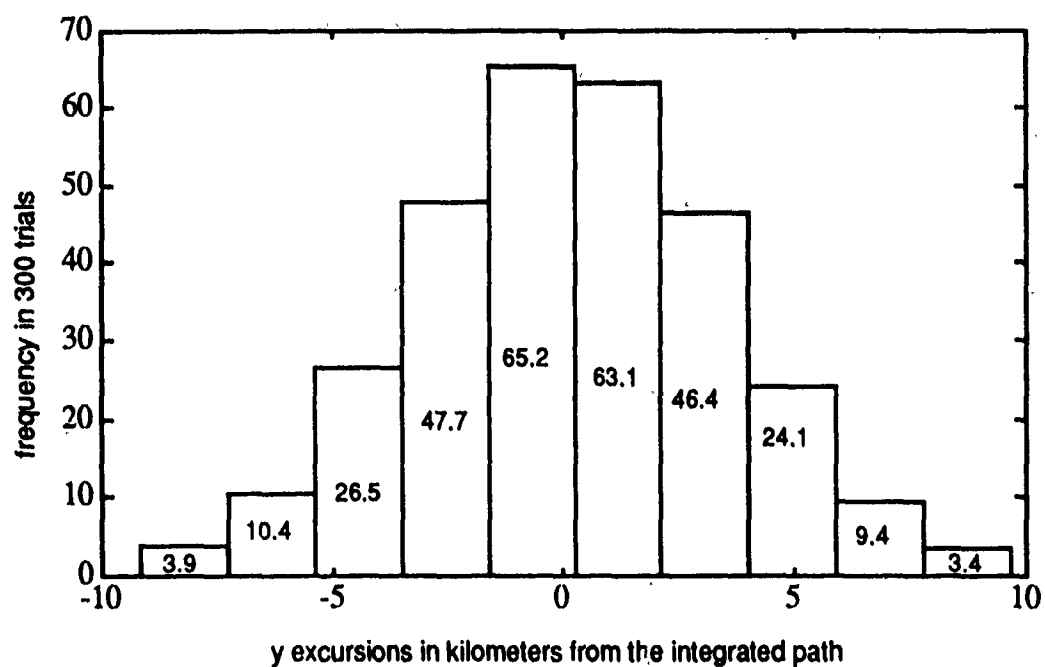
With the completion of both types of statistical tests for the residual state errors, the state errors can be treated as zero-mean Gaussian random variables. Follow-on research incorporating station-keeping simulations may use these characteristics to model the random errors, and the magnitudes of the residual state errors used for the Lissajous and halo-type orbit simulations may be as depicted in Table 5. The solar reflectivity uncertainty can be input as a separate random variable with a standard deviation of 13%, as depicted in Table 1. In station-keeping simulations, the propellant used for a period of station-keeping can be treated as a random variable and subjected to statistical tests similar to those used in this section.



mean = .1566

standard deviation = 3.3477

Figure 3-11. Histogram of y Excursion From Integrated Path Including Observed Frequencies.



mean = .1566

standard deviation = 3.3477

Figure 3-12. Histogram of y Excursion From the Integrated Path Using Gaussian Expectations.

LIST OF REFERENCES

1. S.C. Gordon, "Some Results of Adding Solar Radiation Pressure Forces to the Restricted Three-Body Problem," USAFA TR 91-10, September 7, 1991.
2. R.W. Farquhar, "The Control and Use of Libration-Point Satellites," Ph.D. Dissertation, Department of Aeronautics and Astronautics, Stanford University, Stanford, California, July 1968.
3. R.W. Farquhar, "A Halo-Orbit Lunar Station," *Astronautics and Aeronautics*, June 1972, pages 59-63.
4. J.R. Wertz, Editor, *Spacecraft Attitude Determination and Control*, D. Reidel Publishing Co, Boston, 1978.
5. S. Wolf, *Guide to Electronic Measurements and Laboratory Practice*, Prentice Hall, Englewood Cliffs, New Jersey, 1973.
6. R.W. Farquhar and A.A. Kamel, "Quasi-Periodic Orbits About the Translunar Libration Point," *Celestial Mechanics*, Volume 7, 1973, pages 458- 473.
7. D.L. Richardson and N.D. Cary, "A Uniformly Valid Solution for Motion About the Interior Libration Point of the Perturbed Elliptic-Restricted Problem," AAS/AIAA Astrodynamics Specialists Conference, Nassau, Bahamas, July 28-29, 1975, AAS Paper 75-021.
8. D.L. Richardson, "Halo Orbit Formulation for the ISEE-3 Mission," *Journal of Guidance and Control*, Volume 3, Number 6, November-December 1980, pages 543-548.
9. H.J. Pernicka, "The Numerical Determination of Nominal Libration Point Trajectories and Development of a Station-Keeping Strategy," PhD Dissertation, School of Aeronautics and Astronautics, Purdue University, West Lafayette, Indiana, May 1990.
10. H.J. Pernicka, "The Numerical Determination of Lissajous Orbits in the Circular Restricted Three-Body Problem," M.S. Thesis, School of Aeronautics and Astronautics, Purdue University, West Lafayette, Indiana, December 1986.
11. K.C. Howell and H.J. Pernicka, "Numerical Determination of Lissajous Trajectories in the Restricted Three-Body Problem," *Celestial Mechanics*, Volume 41, 1988, pages 107-124.

12. K.C. Howell, Principal Investigator, "Trajectory Design for Libration Point Trajectories and for Double Lunar Swingby Trajectories," Final Report Prepared for Computer Sciences Corporation, December 1987.
13. K.C. Howell, Principal Investigator, "Design of Libration Point Trajectories and Consecutive Lunar Encounter Trajectories," Final Report Prepared for Computer Sciences Corporation, September 1988.
14. H.J. Pernicka, "The Numerical Determination of Libration Point Trajectories, Including Development of Station-Keeping Strategies," Proposal for Dissertation, School of Aeronautics and Astronautics, Purdue University, West Lafayette, Indiana, December 1988.
15. S.C. Gordon, Representing the Nominal Path for an Interior Libration Point Orbit in the Sun-Earth+Moon Elliptic Restricted Three-Body Problem," USAFA TR 91-11, September 7, 1991.
16. J.L. Bell, Private Communication, School of Aeronautics and Astronautics, Purdue University, West Lafayette, Indiana, August, 1990.
17. The MathWorks, 386-Matlab, 21 Eliot Street, South Natick, Ma, 1989.
18. V. Szebehely, *Theory of Orbits: The Restricted Problem of Three Bodies*, Academic Press, New York, 1967.
19. A.E. Roy, *Orbital Motion*, Second Edition, Adam Hilger Ltd, Bristol, England, 1982.
20. E.A. Grebenikov, "On the Stability of the Lagrangian Triangle Solutions of the Restricted Elliptic Three-Body Problem," *Soviet Astronomy*, Volume 8, Number 3, November-December 1964, pages 567-578.
21. J.M.A. Danby, "Stability of the Triangular Points in Elliptic Restricted Problem of Three Bodies," *The Astronomical Journal*, Volume 69, Number 2, March 1964, pages 165-172.
22. A. Bennett, "Characteristic Exponents of the Five Equilibrium Solutions in the Elliptically Restricted Problem," *Icarus*, Volume 4, 1965, pages 177-190.
23. D.L. Richardson, "Analytic Construction of Periodic Orbits About the Collinear Points," *Celestial Mechanics*, Volume 22, 1980, pages 241-253.
24. T. Kailath, "A View of Three Decades of Linear Filtering Theory," *IEEE Transactions on Information Theory*, Volume IT-20, Number 2, March 1974.

25. G. Strang, *Introduction to Applied Mathematics*, Wellesly-Cambridge Press, Wellesley, Massachusetts, 1986.
26. B.D. Tapley, V. Szebehely, Editors, *Recent Advances in Dynamical Astronomy*, B.D. Tapley, "Statistical Orbit Determination Theory," D. Reidel, Dordrecht-Holland, 1988, pages 396-425.
27. H.W. Sorenson, "Least-Squares Estimation from Gauss to Kalman," *IEEE Spectrum*, July 1970, pages 63-68.
28. R.A. Fisher, "On an Absolute Criterion for fitting Frequency Curves," *Messenger of Mathematics*, Volume 41, 1912, page 155.
29. H. Scheffé, *The Analysis of Variance*, John Wiley, New York, 1959.
30. S.F. Schmidt, "The Kalman Filter: Its Recognition and Development for Aerospace Applications," *Journal of Guidance and Control*, Volume 4, Number 1, January-February 1981.
31. A. Gelb, Editor, *Applied Optimal Estimation*, The M.I.T. Press, Cambridge, Massachusetts, 1974.
32. T. Kallath, "A View of Three Decades of Linear Filtering Theory," *IEEE Transactions on Information Theory*, Volume IT-20, Number 2, March 1974.
33. A.E. Bryson, Jr, Y. Ho, *Applied Optimal Control*, Blaisdell Publishing Company, Waltham, Massachusetts, 1969.
34. R.E. Kalman, "A New Approach to Linear Filtering and Prediction Problems," *Journal of Basic Engineering, Transactions of the American Society of Mechanical Engineers*, Volume 82D, March 1960, pages 35-45.
35. R.H. Battin, *An Introduction to the Mathematics and Methods of Astrodynamics*, AIAA Education Series, New York, 1987.
36. R.H. Battin, "Computational Procedures for a Navigation Fix," Appendix B, "Interplanetary Navigation System Study", Report R-273, MIT Instrumentation Laboratory, Cambridge, Massachusetts, April 1960.
37. R.L. Stratonovich, *Modern Analytic and Computational Methods in Science and Mathematics*, American Elsevier Publishing, New York, 1968.
38. R.E. Kalman, R.S. Bucy, "New Results in Linear Filtering and Prediction Theory," *Journal Basic Engineering, Transactions of the American Society of Mechanical Engineers*, Volume 83D., December 1961, pages 95-108.

39. R.E. Kalman, "A New Approach to Linear Filtering and Prediction Problems," *Journal of Basic Engineering, Transactions of the American Society of Mechanical Engineers*, Volume 82D, March 1960, pages 35-45.
40. A. Gelb, Editor, *Applied Optimal Estimation*, The M.I.T. Press, Cambridge, Massachusetts, 1974.
41. B.D. Tapley, G. H. Born, B. E. Schutz, *Satellite Orbit Determination*, University of Texas at Austin, June 1985.
42. G.D. Mistretta, "Preliminary Considerations for an ISEE-C Least Squares Orbit Determination Strategy," Goddard Space Flight Center, Report X-580-5-251, November 1976.
43. J.B. Joyce, S.J. Leszkiewicz, A.F. Schanzle, "Trajectory Determination Support and Analysis for ISEE-3 from Halo Orbit to Escape from Earth/Moon System," AAS Paper 79-128.
44. L. Efron, D.K. Yeomans, A.F. Schanzle, "ISEE- 3/ICE Navigation Analysis," *The Journal of the Astronautical Sciences*, Volume 33, Number 3, July-September 1985, pages 301-323.
45. J. Rodriguez-Canabal, "SOHO Mission Analysis," ESOC Mission Analysis Office, June 1984.
46. Private Communications with J.M. Longuski (School of Aeronautics and Astronautics, Purdue University, West Lafayette, Indiana) and with J. Campbell, L. Efron, and M. Standish (Jet Propulsion Laboratory, California Institute of Technology, Pasadena, California), August 29, 1991.
47. H.S. Heuberger, "Halo Orbit Station Keeping for International Sun-Earth Explorer-C (ISEE-C)," AAS/AIAA Astrodynamics Specialist Conference, Jackson Lake Lodge, Grand Teton National Park, Wyoming, September 7-9, 1977, AAS Paper 77-165.
48. S.R. Schmidt, R.G. Launsby, *Understanding Industrial Designed Experiments*, CQG Ltd Printing, Longmont, Colorado, 1989.
49. C. Simó, G. Gómez, J. Llibre, R. Martinez, "Station Keeping of a Quasiperiodic Halo Orbit Using Invariant Manifolds," Proceedings of the Second International Symposium on Spacecraft Flight Dynamics, Darmstadt, Federal Republic of Germany, 20-23 October 1986.
50. G. Simó, G. Gómez, J. Llibre, R. Martinez, J. Rodriguez, "On the Optimal Station Keeping Control of Halo Orbits," *Acta Astronautica*, Volume 15, Number 6/7, 1987, pages 391-397.
51. J. Neter, W. Wasserman, G.A. Whitmore, *Applied Statistics*, Allyn and Bacon, Boston, 1988.